Doctoral Dissertation (Censored)

博士論文（要約）

Development of multi-directional muography

（多方向ミュオグラフィの開発）

A Dissertation Submitted for the Degree of Doctor of Philosophy
May 2021

令和 **3** 年 **5** 月　博士（理学）申請

Department of Earth and Planetary Science, Graduate School of Science,
The University of Tokyo

東京大学大学院理学系研究科

地球惑星科学専攻

Shogo Nagahara

長原　翔伍

Abstract

Muography is an imaging technique to measure the density of objects by using cosmic-ray muons. This is one of the best observation methods for probing the structure of objects of about 1000m in size. Many volcanic structure surveys have been carried out using this technique (Tanaka et al., 2007a; 2007b; Oláh et al., 2018; Lesparre et al., 2012). This can also be used to obtain a three-dimensional density structure by observing the same volcano from multiple directions. However, the previous studies have been limited to three directions at most (Rosas-Carbajal et al., 2017), and we have not yet been able to perform 3D density structure survey using muographic observations from multiple directions.

The reason why multi-directional muography has not been done is the following issues.

A) Secure enough detectors to observe in multiple directions.
B) Mass production of detectors and establishment of operation methods.
C) Fast processing from observation data to muon tracks.
D) Development of methods for 3-D density reconstruction.

For (A), Morishima et al. (2017b) have already realized muographic observations using a large number of nuclear emulsion films. For (C), Yoshimoto et al. (2017) and Hamada et al. (2012) have developed a fast processing technique for nuclear emulsion observation data, but it had to be optimized for muography. For (D), there is an analysis method by Nishiyama et al. (2014a), but there were some difficulties in performing high-resolution 3D density reconstruction with this method.

In this paper, we have developed (B) and improved (C) and (D). We also conducted a demonstrative observation at Mt. Omuro-yama in Izu Peninsula, Japan.

First, we developed a detector suitable for multi-directional muography. The features of this detector are as follows.

(a) Easy to handle many emulsion films and lead plates for noise reduction.
(b) A special spring plate was developed to provide uniform pressure to reduce the thermal expansion of the film.
(c) Insulation is used to protect the emulsion film from high temperature.

In addition, FOG (Fiber-Optic Gyroscope) was used to measure the direction and attitude of the detector at any location for field operations.

Second, the process of obtaining muon tracks from observed data was improved for muography. In the previous analysis method, the track data of cosmic rays other than muons are mixed into the track data. In this study, we developed a method to select muon tracks from them. Also we confirmed the noise particle rejection capability using simulation. As a result, low-energy particles below 1 GeV, which were shown in Nishiyama et al. (2014b), could be removed. We also developed a method to evaluate variation of the efficiency according to the detector geometry.

Third, we have improved the 3D density reconstruction method using muography. Specifically, we improved the method to reflect the viewing angle of the observed data.

A demonstrative observation was performed at Mt. Omuro-yama to show the possibility of multi-directional muography. Observations were made in three locations in 2018 and eight locations in 2019. First, the muon counts in free sky region were compared to simulations to evaluate whether the observational data were properly acquired. As a result, it was found that the observed muon number was about 10% less than the simulation. The ratio of the observed muon counts to the simulated muon counts was used as the calibration value. The calibration values were applied to obtain a two-dimensional muographic image. We applied our improved 3D density reconstruction method to the observed muon counts.

The error and uncertainty of the obtained density distribution and the appropriateness of the model parameters were evaluated. The resolution was also evaluated by simulation.

For the model parameters, we considered the correlation length l and a priori error of the density σ_ρ in Nishiyama et al. (2014). For l, we constrained the lower limit to 70m based on the consideration of the amount of information in the data and the degree of freedom of the fitting parameters. For σ_ρ, we excluded the cases with densities of less than 0.5 $(\mathrm{g/cm^3})$ or greater than 3.0 $(\mathrm{g/cm^3})$, which are unrealistic volcanic densities. As a result, σ_ρ < 0.5 $(\mathrm{g/cm^3})$ was selected. We also excluded σ_ρ = $0.1(\mathrm{g/cm^3})$ because it was too restrictive and 3D density structure could not be reconstructed. We also confirmed that there was no significant effect on the reconstruction results between l = 70 m and 100 m. We confirmed that between σ_ρ= $0.2(\mathrm{g/cm^3})$ and $0.4(\mathrm{g/cm^3})$, the density contrast changes but the structure does not

change.

Next, we evaluated the error of the density distribution. Three types of errors were evaluated. The first was to determine the propagation of the error in the observed data, which was determined by the posterior variance matrix in the inversion. Second, we evaluated the effect of the initial density assumed in the inversion. Since the initial density was the value of the bulk density of the mountain obtained from muography data, the error of the 3D reconstruction result coming from the initial density was estimated. Third, we evaluated the stability of the data by selecting the data to be used. We performed 3D density reconstruction excluding data from one observation point and compared it to the case where data from all observation points were used. As a result, it was found that when an observation point was removed, the area near the point tended to become denser. The sum of the squares of the three errors was taken as the variance value of the density error.

In order to evaluate the spatial resolution of the obtained density structures, we performed simulations assuming two types of structures. The first is the case where a 100m diameter cylinder exists just below the crater. The second is the case where a plate-like heterogeneity exists from the west to the crater. The reconstruction result appears to be twice as thick and tends to be larger in the center of the mountain.

Based on the obtained 3D density reconstruction results, taking into account the error and resolution estimation, the internal structure of Omuro-yama was interpreted by comparing it with previous studies and high-precision topographic maps. The structure confirmed by the results of muography is as follows. A high-density region existed in the central part of the mountain body, and the high-density region extended to the west. A high-density region was also found in the south-southeast.

From the above, we have constructed a tentative story of the formation process of Omuro-yama, mainly in its final stages, together with the results of topographic readings. First, when most of the mountain body was formed and a lava lake was formed in the summit crater, the expansion of the mountain body formed a dike that went in three directions from the conduit. Westward dike flowed seeping out from the west side of the mountain. The south-southeastward dike erupted a small crater on the south mountainside. Subsequently, most of the lava lake in the summit crater drained back. After the drained back, the area around the conduit remained hot and the welding

progressed to form the high density region in the center of the mountain.

With this research, we established the detectors, installation techniques, and analysis methods necessary for multi-directional muographic observations. We will increase the number of observation directions by conducting similar observations in the very near future, and 3D density reconstruction with higher spatial resolution and precision will become possible.

Contents

本章については、5 年以内に雑誌等で刊行予定のため、非公開。

本章については、5 年以内に雑誌等で刊行予定のため、非公開。

本章については、5 年以内に雑誌等で刊行予定のため、非公開。

1. Introduction

1.1. Volcanological Background

The internal structure of a volcanic body influences the dynamics of volcanic eruptions and records the evolution and history of volcanic activity. One of the important information for understanding eruptive phenomena in volcanoes is the shape of the volcanic conduit.

In particular, the shape of the shallow part of the conduit affects the eruption rate, which is one of the important parameters to determine the eruption style. For example, the vertical change in the diameter of the conduit affects the magma eruption rate and the height of the plume column (Wilson et al., 1980). The shape of conduit also has a significant impact on ashfall prediction simulations (Suzuki et al., 2009). In addition, whether the plume rises to the sky as a plume column or flows down to the ground surface as a pyroclastic flow depends on the shape of the shallow crater and conduit at the time of explosive eruption (Koyaguchi et al., 2018).

The internal structure of volcanoes has been explored using a variety of techniques.

A direct way to observe the interior of a volcano is to look at outcrops exposed by weathering where the interior of the volcano once was. In Geshi et al. (2014), the relationship between the eruption history and magma chamber in remote areas was discussed by outcrop observation and analysis of sampled rocks. Yamamoto (2003) discussed the morphology of lava outflow in scoria cones by making observations at outcrops where the internal structure of many scoria cones can be observed. Calvari et al. (2014) estimated the internal structure of the crater area at Stromboli volcano from the record of eruption history. From these observations, we know that the structure of the shallow part of the volcano varies from volcano to volcano. While such observation of outcrops has the advantage of being able to observe the internal structure in detail, it has the disadvantage of being limited in where it can be done.

On the other hand, many geophysical explorations have been carried out. in places where people cannot directly observe. Subsurface expansion and contraction sources were estimated based on crustal movement observations using tiltmeters and GPS (Hotta, 2019). Observations have also been made using the MT(Magneto-Telluric)

method, which measures the electrical conductivity of the subsurface.

There are various methods of exploration using seismic waves. Giudicepietro et al. (2009) estimated the movement of magma beneath the ground from the hypocenter migration of volcanic earthquakes. Estimation of 3D seismic velocity structure by seismic tomography has also been studied (Nakamichi et al., 2007). Artificial earthquakes have also been used to estimate seismic velocity and reflection cross-sections (Nakamichi et al., 2020).

With these geophysical methods, it was difficult to capture the structure of the very shallow part of the earth, about 100m deep from the surface. On the other hand, the density structure of the shallow crater was revealed by the muography of Mt. Asama (Tanaka et al., 2007a). This method was shown to be suitable for investigating the internal structure of shallow volcanoes.

1.2. Muography

1.2.1. History of Muography Research

The idea of using cosmic ray muons to see through objects already existed in the 1970s. Alvarez et al. (1970) installed a spark chamber in the Chephren Pyramid in Egypt. They measured the flux of cosmic muons through the pyramid and detected the attenuation of the muon intensity caused by the pyramid. They could not find the hidden chamber inside the pyramid, but this experiment demonstrated the feasibility of radiography by measuring the absorption of muons. Subsequently, this technique has come to be used for a various purposes as non-destructive inspection. For example, castles (Minato, 1986), blast furnaces (Nagamine et al., 2005), seismic faults (Tanaka et al., 2011; Miyamoto et al., 2017), caves (Barnaföldi et al., 2012; Cimmino et al., 2019), glacier (Nishiyama et al., 2019), remains (Morishima et al., 2017b) and volcanoes (Nagamine et al., 1995; Tanaka et al., 2007a, 2007b, 2009, 2010, 2014; Nishiyama et al., 2014a, 2017; Oláh et al., 2018; Lesparre et al., 2012; Rosas-Carbajal et al., 2017; Carbone et al., 2014; Carloganu et al., 2013; Ambrosino et al., 2015; Ambrosino et al., 2015; Tioukov et al., 2017).

1.2.2. Principle of muography

Muography is based on measuring the absorption of cosmic-ray muons inside an object. The attenuation of the muon flux depends on the amount of material present along the muon trajectory. The amount of matter is defined as the density length d, which given by

$$d = \int_{\tau} \rho(\xi) d\xi \,, \qquad (1-1)$$

where ρ is the density, τ is the trajectory of muon and ξ is the coordinate measured along the trajectory τ. The unit of density length is "meter water equivalent" $(\mathrm{m.w.e}) = (\mathrm{g/cm^3} \times \mathrm{m})$. The relationship between muon energy and attenuation with density length is well known (Groom et al., 2001). The energy spectrum of the incident muon is well known and it depends on the elevation angle (Honda et al., 2004). Therefore, the penetrate muon flux F $(\mathrm{m^{-2} \cdot sr^{-1} \cdot s^{-1}})$ depends on the density length d and elevation angle Z. Fig. 1.1 shows the penetrate muon flux as a function of the density length and elevation angle. The number of detected muons of i-th solid angle area N can be written as

$$N = T \int_{\Omega_i} S(\Omega) F(d(\Omega), Z(\Omega)) d\Omega \,, \qquad (1-2)$$

Where S is the effective area of the detector, T is the exposure period, Ω is solid angle and Ω_i is the integral range of the solid angle. The elevation angle Z depends on solid angle because the integral in the solid angle is the integral with respect to the direction of arrival of the muon. the effective area S also depends on solid angle because the effective area differs in each direction depending on the device shape (Fig. 1.2). When observation condition of muon (S, T) and the integrated range of the solid angle are the same, N_i depends on only density length d and N_i is a monotonous decrease. When Ω_i is sufficiently small to neglect the density length change within Ω_i, d can be written as

$$d = f(N). \qquad (1-3)$$

The passing distance of an object along the muon trajectory τ is defined as the path length p. In the case of volcanic observations, p can be obtained from topographic data. The average density in the τ direction can be obtained by dividing d by p.

When the observed muon counts are small, Ω_i needs to be increased until sufficient muon statistics are obtained. When Ω_i is large, it is impossible to detect the density

length variation in Ω_i from N_i. In this case, an assumption is needed to determine the physical quantity of the object from the observed muon counts. The simplest assumption is that it is uniform within Ω_i. However, it is not suitable to assume that the density length in Ω_i is uniform because density length is dependent on topography (Fig. 1.3). So, we assumed that the density of objects along the path in the solid angle Ω_i was uniform. Then, the number of detected muons of i-th solid angle area N_i can be written as

$$N_i = T \int_{\Omega_i} S(\Omega) F(\rho_i \cdot p(\Omega), Z(\Omega)) d\Omega \,, \qquad (1-4)$$

where ρ_i is the mean density in Ω_i. In equation (1-4), the unknown parameter is only ρ_i, so ρ_i can be written in the same form as in Equation (1-3) as

$$\rho_i = g(N_i). \qquad (1-5)$$

In principle, it is possible to make Ω_i a whole image of muography. This is equivalent to assuming that the density of the object is uniform. However, we note that when the object has a non-uniform density distribution, the bulk density of the object and the density obtained by assuming that the density is uniform do not equal. This is because when Ω is taken too wide, the difference between solid angle area with large muon counts and small muon counts within Ω becomes large. In muography, the observed muon count increases with decreasing path length. The higher the elevation angle, also the higher the flux (Fig. 1.1). On the other hand, the contribution to the bulk density is larger for longer path lengths. Therefore, the location in the object where the contribution to the muon count is large is different from the location in the object where the contribution to the bulk density is large.

From the above, when determining the bulk density of an object, it is necessary to separate Ω_i as small as possible and determine the average density by considering the contribution to the bulk density at each Ω_i. The contribution of the solid angle area Ω_i to the bulk density is the volume of the object carved out by Ω_i. Therefore, the bulk density of the object can be obtained by

$$\overline{\rho} = \frac{\sum_i \rho_i V_i}{\sum_i V_i}, \qquad (1-6)$$

where $\overline{\rho}$ is the bulk density of object, V_i is the volume of the object carved out by Ω_i.

Since the observed muon counts N follows a Poisson distribution, the error is represented by $\sqrt{N}$. Since $g(N)$ is nonlinear, the error range of the mean density is

different on the upper and lower sides. Therefore, the error in the mean density $\delta\rho$ was defined below as a typical value, assuming that the relationship between the observed muon count and the mean density is linear from $N-\sqrt{N}$ to $N+\sqrt{N}$.

$$\delta\rho = \frac{g\left(N-\sqrt{N}\right) - g\left(N+\sqrt{N}\right)}{2}. \qquad (1-7)$$

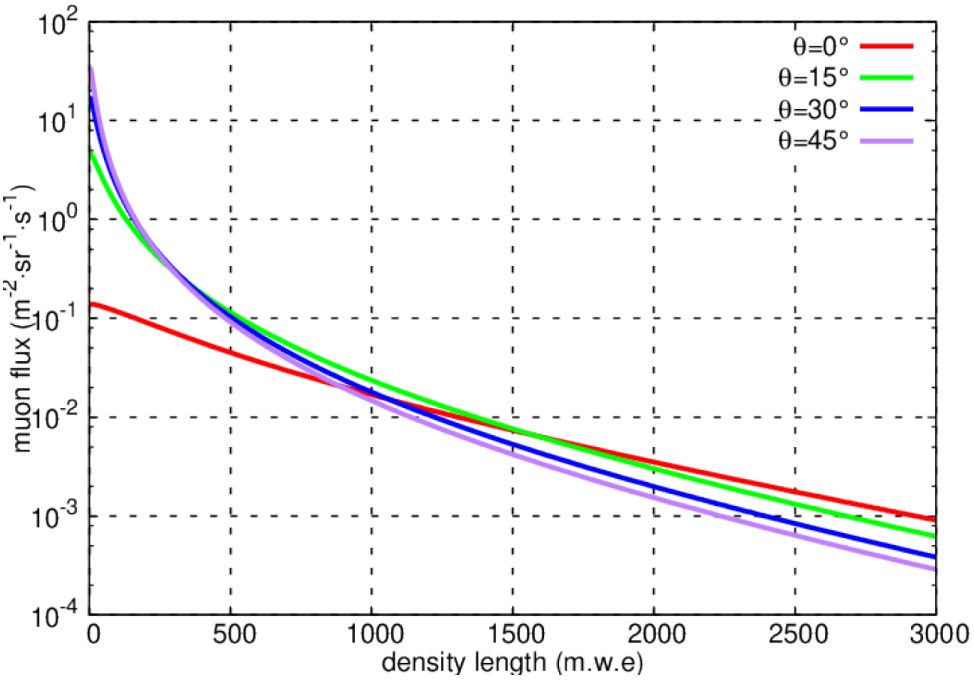

Figure 1.1: Penetrate muon flux as a function of the density length for four elevation angles. θ is elevation angle.

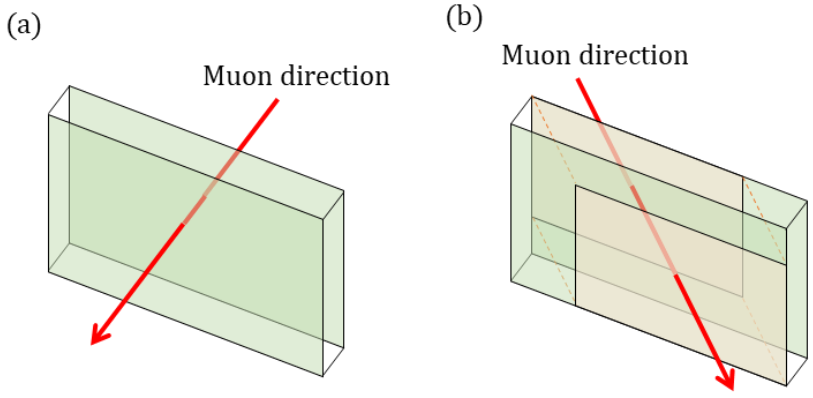

Figure 1.2: Schematic view of the effective area. We assume that the muon that passes through both of the two green plates is detected. (a) When the muon comes from the front of the detector, the whole green plate is the effective area. (b) When the muon comes from an angle, Only the orange area is the effective area that passes through the two plates.

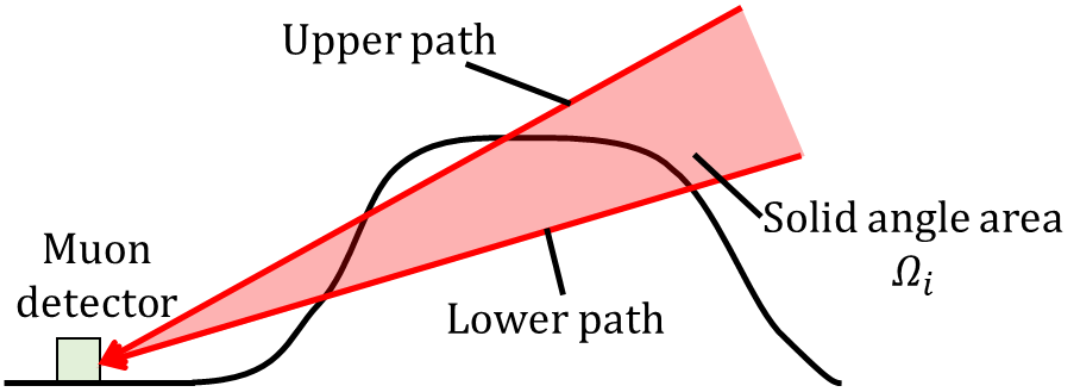

Figure 1.3: Schematic view of Density length in Ω_i. The path length in the solid angle area Ω_i varies from the upper path to the lower path. Assuming that the density length in Ω_i is uniform is equivalent to assuming that the longer the path length, the lower the density. Since the path length can vary several times even within Ω_i, this assumption is unnatural because it assumes that the density of the object also varies several times.

1.3. 3-D density reconstruction for muography

1.3.1. History of 3-D density reconstruction for muography

Tanaka et al. (2010) is the first example of attempting a three-dimensional density reconstruction using muography data. They performed muography from two directions at Mt. Asama, Japan and they attempted to estimate the location of the conduit. Nishiyama et al. (2014a) performed a three-dimensional density reconstruction by combining muography and gravity data. They developed a method that combines a priori information about spatial correlation and they applied it to Showa-Shinzan, Usu, Japan. The various model of spatial correlation have been proposed (Exponential decay: Nishiyama et al., 2014a; Gaussian model: Barnoud et al., 2019; Layered Structure: Cosburn et al., 2019). Rosas-Carbajal et al. (2017) is one of the most extensive observations. They used muography from three directions and gravity data for 109 points at La Soufrière de Guadeloupe lava dome.

Analysis methods have been developed by using numerical simulation. Jourde et al. (2015) developed a processing method for muon flux data that varies nonlinearly with density. Barnoud et al. (2019) evaluated and proposed a method for determining parameters regarding a priori information. Nagahara et al. (2018) proposed the method

of filtered back projection. Compared to inversion, this method has the advantage that it does not require a priori information, but on the other hand, it has the disadvantage that systematic errors increase when the number of observations is small.

1.3.2. The Method of 3-D density Reconstruction

In this section, we discuss the method for 3-D density reconstruction by Nishiyama et al. (2014a).

Suppose the region of reconstruction is subdivided into J voxels of density ρ_j $(j = 1,2,\dots,J)$. Here, density length of path i $(i = 1,2,\dots,I)$ is written as follows.

$$d_i = \sum_{j=1}^{J} A_{ij}\,\rho_j, \qquad (1-8)$$

where d_i is density length of path i, A_{ij} is the length of the i-th path across the j-th voxel. Equation (1-8) can be written as follows:

$$\boldsymbol{d} = \mathbf{A}\boldsymbol{\rho}, \qquad (1-9)$$

where $\boldsymbol{d}$ is the data vector, $\mathbf{A}$ is the observation matrix, $\boldsymbol{\rho}$ is the voxel densities. Fig. 1.4 shows schematic view of observation matrix for muography.

Solving equation (1-9) for $\boldsymbol{\rho}$ is a linear inverse problem. Nishiyama et al. (2014a) proposed a method for incorporating a priori information based on Bayesian approach (Tarantola et al., 1982). Nishiyama et al. (2014a) assumed the following two things. First, the true value data $\boldsymbol{d}$ is described by a Gaussian probability density function (pdf) with observation $\boldsymbol{d_{Obs}}$ and a covariance matrix $\mathbf{C_d}$. Second, a priori information on model parameters is also described by a Gaussian pdf with initial guess density $\boldsymbol{\rho_0}$ and a covariance matrix $\mathbf{C_\rho}$. The model expectation $\boldsymbol{\rho'}$ and its posterior covariance matrix $\mathbf{C_{\rho'}}$ is obtained when posterior Gaussian function have peak,

$$\boldsymbol{\rho'} = \boldsymbol{\rho_0} + \left({}^{t}\mathbf{A}\mathbf{C_d^{-1}}\mathbf{A} + \mathbf{C_\rho^{-1}} \right)^{-1} {}^{t}\mathbf{A}\mathbf{C_d^{-1}}(\boldsymbol{d_{Obs}} - \mathbf{A}\boldsymbol{\rho_0}), \qquad (1-10)$$

and

$$\mathbf{C_{\rho'}} = \left({}^{t}\mathbf{A}\mathbf{C_d^{-1}}\mathbf{A} + \mathbf{C_\rho^{-1}} \right)^{-1}. \qquad (1-11)$$

Nishiyama et al. (2014) imposed a smoothing constraint through an exponential covariance on $\mathbf{C_\rho}$ based on Tarantola et al. (1984);

$$\mathbf{C}_{\boldsymbol{\rho}}(j_1, j_2) = \sigma_\rho^2 \exp\left(-\frac{D(j_1, j_2)}{l}\right), \qquad (1-12)$$

where σ_ρ is a priori error of the density, l is the correlation length, and $D(j_1, j_2)$ is the distance between j_1-th voxel and j_2-th voxel.

In equation (1-10) and (1-11), data covariance matrix $\mathbf{C}_{\boldsymbol{d}}$ represents observation error. In case of muography, density length is independently for each muon path, so data covariance matrix is a diagonal matrix

$$\mathbf{C}_{\boldsymbol{d}}(i_1, i_2) = \begin{cases} \sigma_{d,i}^2 \ (i_1 = i_2 = i) \\ 0 \ (i_1 \neq i_2) \end{cases}, \qquad (1-13)$$

where $\sigma_{d,i}$ is the error of density length of i-th path. From eq. (1-3), σ_d is expressed as

$$\sigma_d = \frac{\partial f}{\partial N}(N_{Obs})\delta N, \qquad (1-14)$$

where N_{Obs} is the number of detected muons and δN is the standard deviation (SD) of the muon count. Since the arrival of cosmic-ray muons to the detector is a rare and random process, the statistical fluctuations in the number of muons is governed by the Poisson distribution. So $\delta N = \sqrt{N_{Obs}}$.

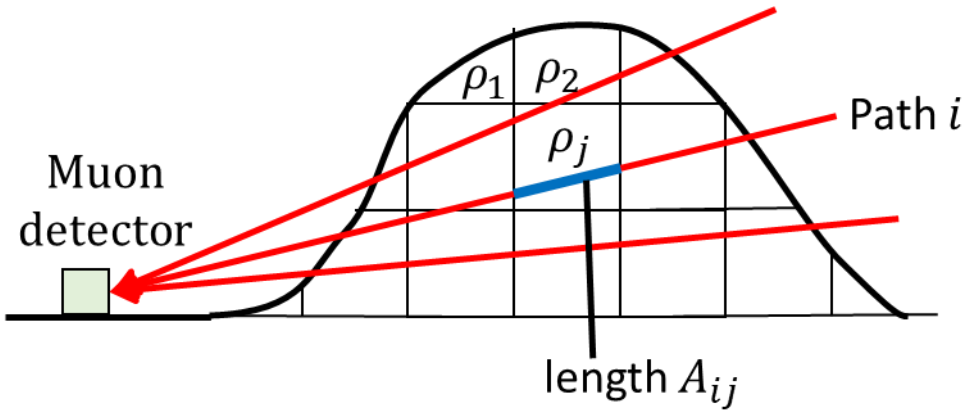

Figure 1.4: Schematic view of observation matrix for muography.

1.3.3. Problems in 3D Density Reconstruction with Muography

All of the 3D density reconstructions that have been done so far using muography have resolutions of more than 100 meters (Rosas-Carbajal et al. ,2017; Nishiyama et al., 2017). However, some of the sizes assumed in volcanic structures are smaller than this. For example, the conduit size estimated by Calvari et al. (2014) and the width of the dike observed by Geshi et al. (2014) are less than a few tens of meters. On the other hand, simulations by Nagahara et al. (2018) showed that a resolution of at least 20 m can be obtained if the number of observation points is increased sufficiently (60 view points). The maximum number of observation points in the muographic observations that have been conducted so far is three (Rosas-Carbajal et al. ,2017). It is necessary to develop the technology to perform multi-directional muography with more observation points.

1.4. Problems for the realization of multi-directional muography

1.4.1. Emulsion Cloud Chamber: Detectors suitable for multi-directional muography

For muography, various types of detectors have been used. In this section, we discuss the features of the detector required for multi-directional muography and the detector suitable for it.

For muography, various types of detectors have been used, such as scintillation detectors (Tanaka et al., 2009; Tanaka et al., 2010; Lesparre et al., 2012; Tanaka et al., 2014; Carbone et al., 2014; Rosas-Carbajal et al., 2017; Saracino et al., 2017), gas chamber detectors (Barnaföldi et al., 2012; Carloganu et al., 2013; Olah et al, 2018) and nuclear emulsions (Tanaka et al., 2007a, b; Nishiyama et al., 2017; Tioukov et al., 2017; Nishiyama et al., 2019).

The advantage of scintillation detectors and gas chamber detectors is that they allow for real-time observations. For example, Tanaka et al. (2014) used a scintillator detector at Satsuma-Iwo Jima to capture magma head changes as time-lapse movies every three days. At Soufriere volcano, scintillator detectors have also detected changes in the groundwater level due to hydrothermal systems on a weekly time scale (Jourde et al., 2016). On the other hand, since these detectors require a power supply, there are

limitations on where they can be installed. This limitation can be a fatal weakness in performing multi-directional muography.

On the other hand, nuclear emulsions do not require a power supply. In addition, the resolution of muon trajectories in nuclear emulsion is 1000 times higher than that of scintillation detectors and gas chamber detectors. For example, scintillation detectors and gas chambers have a positional resolution of 2 to 4 mm (Saracino et al., 2017; Olah et al, 2018), but nuclear emulsions have a positional resolution of 1 micrometer (Yoshimoto et al., 2017). Therefore, when detecting the displacement due to multiple Coulomb scattering and eliminating low-energy particles, nuclear emulsions require less weight of the scatterer. On the other hand, nuclear emulsion has the following disadvantages: first, real-time observation is not possible; second, it takes a long time to obtain a muographic image because it is necessary to develop and process the recorded trajectory image after the observation.

The most important feature of the detectors used in multi-directional muography is that they can be installed in any location. From this point of view, the use of nuclear emulsion is appropriate for multi-directional muography.

Nuclear emulsion has three layers: an emulsion gel, a plastic base and an emulsion gel. Typically, the thicknesses are 50-80μm for gel and 180-210μm plastic base. The main components of the gel are AgBr crystals and gelatin. When a charged particle passes through the gel layer, latent images are created nearby the trajectory of the particle. After chemical development, these latent images become sub-micron silver grains. The three-dimensional line that connects silver grains is the trajectory of the charged particle. The line of silver grains is read by automated microscope (Yoshimoto et al., 2017).

The nuclear emulsion degrades in hot and humid environments since latent images fade (Nishio et al., 2012; Morishima et al., 2017a). In case of muography for volcano, it is important to keep the films at a low temperature because they are installed outdoors. For this reason, many of muography using nuclear emulsion was observed during the winter months (Nishiyama et al., 2017; Tioukov et al., 2017).

The observation of nuclear emulsion is contaminated by background noise arising from low-energy charged particles. Nishiyama et al. (2014b) revealed by test measurements that contamination of nonsignal particles with low-energy ($<\approx 1$GeV)

caused systematic errors for the density estimation of muography. Nishiyama et al. (2016) identified the origins of those background particles. To reduce the background noise, Nishiyama et al. (2017) used the multilayer detector with thin lead (1-mm-thick) plates inserted between emulsion films.

1.4.2. Problems for the realization of multi-directional muography

It is difficult to realize multi-directional muography by simply performing conventional muography with nuclear emulsion at multiple observation points. In this section, we overview the observations made by Nishiyama et al. (2017) as an example of muography performed on a volcano. After that, the problems in realizing multi-directional muography are clarified, and the recent researches for them are described.

Amount of emulsion films

Nishiyama et al. (2017) used 20 pieces of nuclear emulsion film of 12.5 cm × 10.0 cm. Multi-directional muography requires a large amount of film. In recent studies, Nagoya University has set up a mass production system for emulsion film. As a result, Morishima et al. (2017b) was able to use $8\mathrm{m}^2$ emulsion films. Therefore, the supply system of emulsion films required for multi-directional muography is already in place.

Detector configuration

Nishiyama et al. (2017) used a specially made detector that was not intended for mass production. In addition, the process of layering the lead plate and film for background noise reduction was done manually. In multi-directional muography, it is necessary to have multiple detectors. Also, if the film and lead are misaligned, the effective area becomes smaller. Therefore, it is necessary to develop a detector that can be mass-produced and can easily and reliably adjust the position of film and lead.

Method for measuring the azimuth and slope of a detector

Nishiyama et al. (2017) used triangulation to measure the orientation and attitude of the detector. In multi-directional muography, the reference points that can be used for

triangulation do not always exist near the observation points. Therefore, it is necessary to adopt an orientation and attitude measurement method that is independent of the installation location.

Developing

In Nishiyama et al. (2017), all the emulsion films were developed in F-lab, Nagoya University. The method for developing large amounts of film has already been established (Morishima et al., 2017b).

Scanning

In Nishiyama et al. (2017), the tracks recorded in the emulsion films were read using ESS (European Scanning System) (Arrabito et al., 2006). The scanning speed of ESS was 20 cm^2/h. Currently, HTS (Hyper track selector) with a scanning speed of 7000 cm^2/h is being developed (Yoshimoto et al., 2017).

Track reconstruction

In Nishiyama et al. (2017), the track data was processed using FEDRA (Framework for Emulsion Data Reconstruction and Analysis) (Tioukov et al., 2006). Currently, the next generation of the track reconstruction framework called “NETSCAN2.0” is being developed (Hamada et al.,2012). This framework is high-speed and can process a large number of films used in multi-directional muography.

However, since this framework also reconstructs tracks other than cosmic ray muons used in muography, it is necessary to develop a processing method to select the muon tracks.

3-D density reconstruction

In Nishiyama et al. (2017), the method of Nishiyama et al. (2014) was used for 3D density reconstruction. This method has the following points that can be improved.

1. Clarifying the treatment of areas where voxels are not defined.
2. Consideration of solid angle area of muon arrival direction.

Especially, the second point needs to be improved because it affects the resolution of the reconstruction result.

From the above, the elements that need to be developed for the realization of multi-directional muography can be summarized as follows.

A) Development of a detector suitable for multi-point installation and its operation method.
B) Development of a method to select muons for muography from reconstructed tracks.
C) Improved method for 3D density reconstruction.

In this study, we developed them.

1.5. Demonstration observation of multi-directional muography

1.5.1. Conditions required for demonstration targets of multi-directional muography

Demonstration observations are needed to confirm that what we have developed for multi-directional muography is practical. The following conditions are required for a suitable observation target for multi-directional muography.

(1) The size should be suitable for muography.
(2) No reflection of other structures such as mountains in the background in any direction.

In addition, it is more suitable for demonstration observation if the observation target satisfies the following conditions.

(i) Anisotropy in the internal structure is expected.
(ii) Easy access to the observation point.

Mt. Omuro-yama was selected as an observation target that satisfied the above criteria.

1.5.2. Volcanological Backgrounds of Mt. Omuro-yama

Mt. Omuro-yama (34°54’11’’N, 139°05’40’’E, 580 m asl.) is a scoria cone formed by a single eruption located in Izu Peninsula, Japan. The mountain baseline diameter is about 1 kilometer and the height from base is 300 meters (Fig. 1.5). At the top of the

mountain, there is a crater 300 meters in diameter and 50 meters deep. Saito et al. (2003) estimated that the eruption occurred approximately 4Ka using radioactive carbon dating.

The eruption has been investigated by volcanic products surveys (Koyano et al.,1996). This eruption extruded a large amount of lava flow. Koyano et al. (1996) estimated the total amount of lava flow to be 10^8 m^3. Fig. 1.6 shows the lava flow of Mt. Omuro-yama. The main lava flows were lava flow II (78.0×10^6 m^3) from northeastern feet of the cone and lava flow III (14.7×10^6 m^3) from the southern of the cone. Focusing on the area around Mt. Omuro-yama scoria cone, there was a lava flow from western side of the cone (lava flow IV). Traces of a lava lake were found in the summit crater.

In 2019, high-precision DEM measurements of 10 cm mesh were made in eastern Izu, including Mt. Omuro-yama (Suzuki et al., 2020). From this data, we obtained the following information and consideration. Fig. 1.7 shows the results of the DEM reading. The topography of the western part of the summit crater was complex, including a depression near the northern edge of the crater rim that was considered to be a small crater, and a small pyroclastic cone to the south of the depression. As for the topography other than the summit area, we can clearly confirm the topography of lava flow IV (Koyano et al., 1996) and its southwestern extension, which seeped out from the base of the mountain at the end of the eruption.

Thus, the interior of Mt. Omuro-yama scoria cone is expected not to be a simple axial structure with the summit crater as its axis.

The lava of Mt. Omuro-yama is a basaltic andesite with 54 to 56 wt% SiO_2 (Hamuro, 1985). In general, the density of these rocks is 2.5 to 3.0 (g/cm^3). The density of the densely welded part of Mt. Omuro-yama is expected to be around this value. On the other hand, the density of the sedimentary parts of the scoria depends on the degree of foaming of the sediment. Although the degree of foaming of scoria in the Mt. Omuro-yama has not been measured, Koyano et al. (1996) mentioned that the volcanic ejecta during the period when Mt. Omuro-yama was formed has good foaming. Therefore, the density of the non-welded part of the Mt. Omuro-yama scoria cone is estimated to be 1.0 to 1.5 (g/cm^3).

On the other hand, the size of the welded portion inside the scoria cone varies.

Yamamoto (2003) mentioned that the internal structure of scoria cone can be grouped according to the degree of welded. When the degree of welded is high, a welded layer with a diameter as large as that of a summit crater may form around the conduit. Yamamoto (2003) also noted that the higher the degree of welded, the less likely of landslide. Mt. Omuro-yama is a large mountain with a diameter of about 1 km, but it has not occurred landslide. Therefore, it is expected that the inside of the mountain is welded. The crater diameter of Mt. Omuro-yama is about 300 m, and the crater bottom is also about 100 m in diameter, so the welded around the conduit is expected to be about 100 m in diameter.

From the above, it is sufficient to detect structures with a density difference of 0.5 (g/cm^3) and a diameter of about 100 m to estimate the internal structure of Mt. Omuro-yama.

Figure 1.5: The picture of Mt. Omuro-yama from northwestern side (photo's by Koyama).

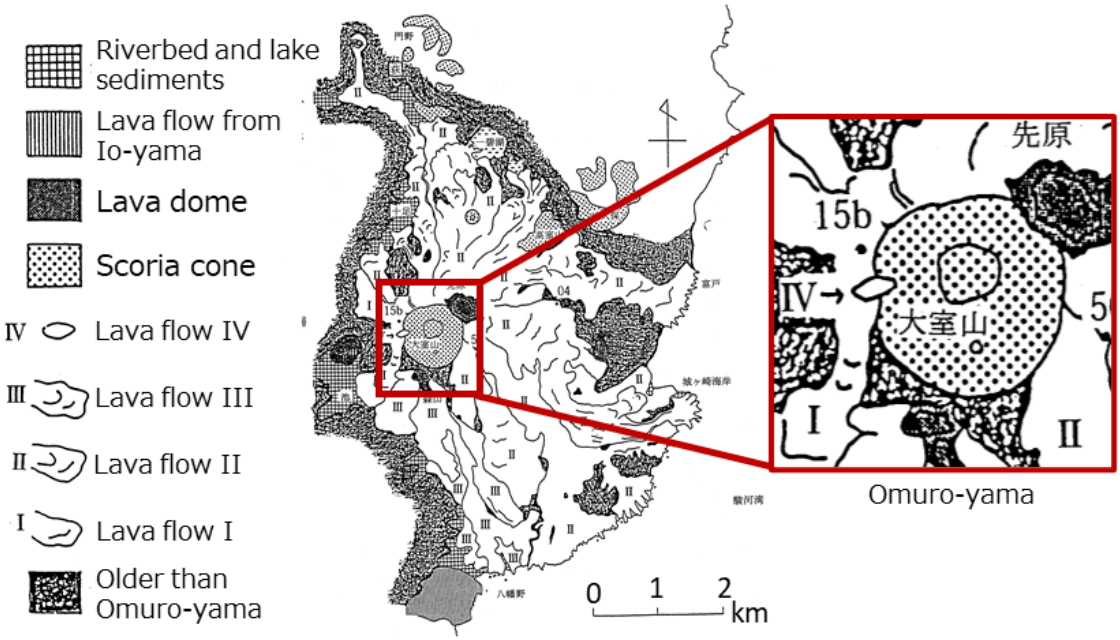

Figure 1.6 : Lava flow of Mt. Omuro-yama. Modified figure 5 in Koyano et al. (1996).

本画像は 5 年以内に雑誌等で刊行予定のため、非公開。

Figure 1.7: (a) Zoomed-in view of the crater area. Green represents a small crater. The pink area represents small pyroclastic cone. The blue area represents the base of the summit crater. The purple areas represent the traces of lava lakes. The red area indicates a strongly welded area. (b) Lava flow on the west side of the mountain. Races of lava flows were found in a wider area around the lava flow IV of Koyano et al. (1996). Lava flow is drawn by Koyama.

1.6. Overview

In Chapter 2, we describe the new development in this research for the realization of multi-directional muography. Specifically, Section 2.2 discusses the development of the detector and its operation. In section 2.3, we describe how to select the muon tracks to be used in the muography from the analysis data of emulsion films and how to estimate the efficiency of the detector. In section 2.4, improvements to the 3D density reconstruction method are described. In Chapter 3, we describe the results of the demonstration observations. In Chapter 4, the 3D density reconstruction results were discussed. Specifically, three topics were discussed: the selection of parameters to be used for 3D density reconstruction calculations, the evaluation of errors including systematic errors that depend on the 3D density reconstruction calculation method, and the evaluation of resolution by simulation. In Chapter 5, we interpret the internal structure of Mt. Omuro-yama and its eruptive history based on the 3D density reconstruction results and previous studies. In chapter 6, the future prospects of this research are described. Chapter 7 summarizes the whole study.

2. Development of multi-directional muography

2.1. Overview

In this chapter, we focus on the actual developments that have been made to realize multi-directional muography. In the section 2.2, we describe the detector developed for multi-directional muography and its actual operation. In the section 2.3, we describe the method we have developed for selecting muons for muography from the reconstruction track, the corresponding noise cut estimates, and the calculation of detection efficiency. In the section 2.4, we describe improvements to the 3D density reconstruction method.

2.2. Development of detectors and observation techniques

In multi-directional muography, a large number of observation points are installed. The following conditions must be met in order to perform observations with a sufficient number of observation points.

Development of detectors that can be mass-produced and are easy to handle

In previous study, it required manual adjustments on site when building up the ECC (For example, Nishiyama et al., 2017). In multi-directional muography, it is better to stabilize and increase the quality of all detector measurements. To do it, we developed a special container to store the film and lead.

How to measure the orientation and the angle of the detector

In multi-directional muography, it is necessary to be able to measure azimuth and slope of the detector regardless of the installation location.

In this section, these are described in order.

2.2.1 Test observation in 2018

Prior to the full-scale observation, a test observation was conducted at Mt. Omuro-yama in 2018. The purpose of this observation is to identify again the issues that need to be resolved by conducting small-scale observations prior to full-scale

multi-directional muographic observations.

2.2.1.1. Emulsion Cloud Chamber

The detector used in this observation was configured as follows.

The films consist of a 200-μm-thick plastic base and 80-μm-thick emulsion gel on both sides of the base. These ones are of the same quality as the ones used by Morishima et al. (2017b). The size of film used for this observation is 12.5 cm × 10.0 cm. The film was vacuum packed in a shading bag. To reduce the background noise, used the multilayer detector with thin lead (1-mm-thick) plates inserted between emulsion films. We use the same size lead as the film. We stacked 20 sheets of film and 19 sheets of lead plates per ECC. We used 3 pieces of ECC. The total number of films is 60 sheets.

In order to simplify the positioning of the film and lead plate, one film and one lead plate were fixed with spray glue. Twenty of these were prepared, and the positions of the films were manually adjusted in the field. This platform has four legs, which were adjusted to make the platform horizontal.

Observations using this detector obtained muographic images (See Chapter 3). However, The following issues were found in increasing the number of observation points for multi-directional muography.

Film and lead positioning

When the positions of the ECC films and lead are displaced from each other, the effective area of the ECC becomes smaller. Therefore, it is necessary to conveniently align the lead with the film on site. The present method sufficiently achieved the goal of fixing the position of the film and the lead plate. However, there remained a problem in adjusting the position between the films. Initially, it was planned to adjust the position of the films according to the lead plate to which they were attached, but it was difficult to check the position of the lead plate due to the surrounding work environment. In addition, when peeling off the glue from the film and lead plate after the observation, some of the films were overloaded and broke.

Thermal Expansion of Film

When the emulsion gel expands thermally, the position of the tracks is displaced. To prevent this, the entire film needs to be pressurized above 1 atm. However, in this observation, since the compression was done manually in a vise, it depended on the operator's senses to determine whether the compression was sufficient or not.

2.2.1.2. Installation Method

In this observation, the installation work was done in the following way.

1. Digging a hole for burial.
2. Measure the orientation of the case using FOG (Fiber-Optic Gyroscope).
3. Put the case for the detector into the hole.
4. Install the film.
5. Bury the case.

The following issues were found in the observations made at this time.

Latent images fading

The nuclear emulsion degrades in hot and humid environments since latent images fade (Morishima et al., 2017a). Typically, the temperature of the film must be maintained below 25°C. In this observation, we tried to suppress the temperature rise by burying the detectors underground. However, in this observation, the detector was only shallowly buried, and the temperature of the detector was close to the outside temperature.

The azimuth and slope of the ECC

In this observation, the attitude of the detector was adjusted on the installation table to be horizontal. However, there was a case where the detector could not be installed horizontally and its position was moved from the original plan when the installation location was examined in the field. In multi-directional muography, we may not always be able to choose the easiest place to install the detector because there are many observation points. Therefore, the azimuth and slope of the detector may not always be fine-tuned.

The orientation of the detector was measured in two steps. First, the orientation of the box containing the detector was measured using a Fiber-Optic Gyroscope (FOG), and then the deviation between the orientation of the detector placed in the box and the orientation of the box was measured using a protractor with a scale of 0.5 degree.

2.2.2 Observation in 2019

The detector and installation method for the 2019 observations was developed based on the issues identified in the 2018 observations. Table 2.1 shows the issues identified in the 2018 test observations and their solutions.

Table 2.1: The issues identified in the 2018 test observations and their solutions.

The issues in the 2018 observation	The solutions in 2019 observation
Film and lead positioning	We developed a new ECC specifically for this purpose to solve the problem. (2.2.2.1)
Thermal Expansion of Film	
Latent images fading	The ECC was covered with insulation and buried underground to reduce the temperature rise. (2.2.2.1)
The azimuth and slope of the ECC	The azimuth was measured using Fiber-Optic Gyroscope (FOG) and the slope was measured using a digital level. (2.2.2.2)

2.2.2.1. Emulsion Cloud Chamber

In this observation, the same film and lead plates were used as in 2018. We stacked 20 sheets of film and 19 sheets of lead plates per ECC. We used 16 pieces of ECC. The total number of films is 320 sheets. The emulsion film used in this study was an existing one. For example, Morishima et al.(2018) used these types of emulsion films.

We developed this container to solve the problems at the time of observation in 2018. The basic structure of the ECC is the same as Nishiyama et al. (2017), with alternating layers of emulsion film and lead plates to distinguish low-energy noise components. The ECC in this study is a modified version of this structure that can be easily used in the field. A container consists of the following four parts.

Outer case

Fig. 2.1 shows the drawing and the picture of outer case of container. Cases for ECC have been used in the previous study (Miyamoto et al., 2017). The case of this study was improved by reviewing the structure from scratch so that the aluminum frame described below could be inserted.

The case is made of aluminum to save weight. On the back, there are bolt holes for applying pressure using plates with springs (discussed below). The case can be joined horizontally with supporting parts. This allowed us to easily line up multiple ECCs to increase the effective area. In this observation, we used two joined ECCs. Because this container is rectangular, we can measure the slope of the container by holding a level against the top plate. For the measurement of azimuthal angle, we made an attachment that fixes the relative position of the container with FOG.

Frame for film holding

To hold the film and lead, a specialized aluminum frame was created. The structure of using an aluminum frame to fix the film and lead and to adjust their relative positions is original to this study.

The aluminum frame is made of a 1 mm thick plate with a hole the same size as the lead plate in the center. We taped the lead plates to this frame and taped the film (Fig. 2.2). We can do all this work in the laboratory before the observation. Using this plate, we were able to handle one lead plate and one film in one piece. The positions of the plates can be easily aligned by pulling the aluminum frame to the inner wall of the outer case.

When we reconstructed a track that went through multiple films, muon tracks that have passed through at different relative positions between the films are not connected. To distinguish between non-observational tracks, the position of the aluminum frame was shifted except during observation (Fig. 2.3).

Plates with springs

To apply pressure across the film, we prepared a spring-loaded plate (Fig. 2.3). The structure of using a plates with springs to compress the film is original to this study.

After putting this part into the outer case, we are able to apply pressure by tightening the bolts from behind. We can adjust the pressure by putting a 1-mm thick plastic plate

in the case.

Insulation cover

To prevent temperature rise, we created an insulation cover to cover the outer case. To avoid direct sunlight, we buried the ECC. Temperature monitoring of ECC has been done in previous studies (Nishiyama et al., 2017; Miyamoto et al., 2017). However, in this study, observations were made until the period when temperatures were higher than in previous studies. Therefore, insulation was added as a safety measure.

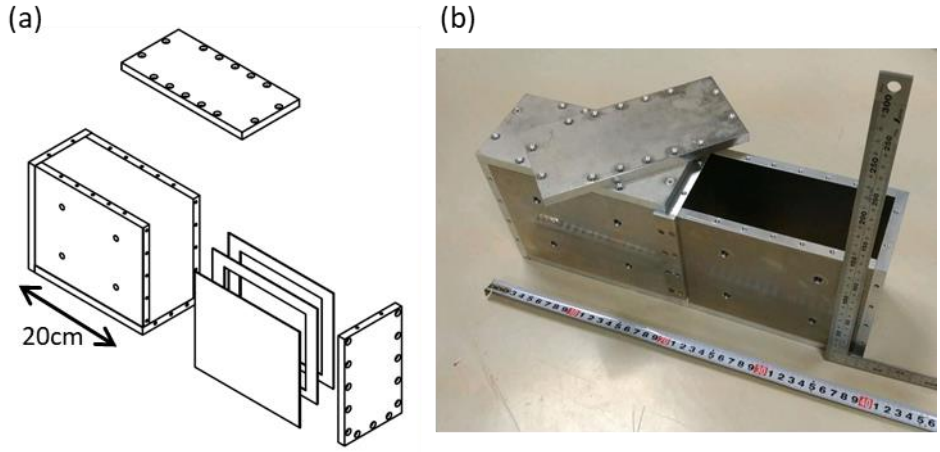

Figure 2.1: The drawing and the picture of outer case of container. (a) The drawing of outer case of container and aluminum frame. (b) The picture of outer case of container. The container can be connected to the left and right. The photo shows two ECCs connected together.

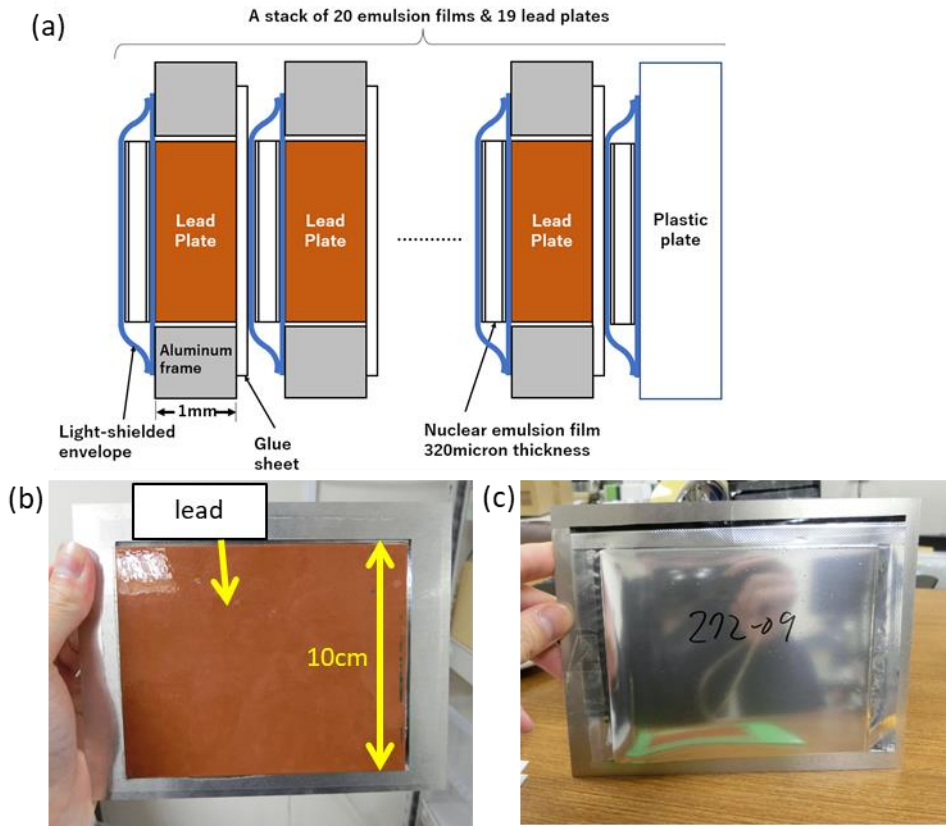

Figure 2.2: The aluminum frame and emulsion film. (a) Schematic figure Schematic diagram of the position of the aluminum frame during transport and observation of aluminum frame and film. (b) The aluminum frame and lead plate. (c) Picture of the film attached to the aluminum frame.

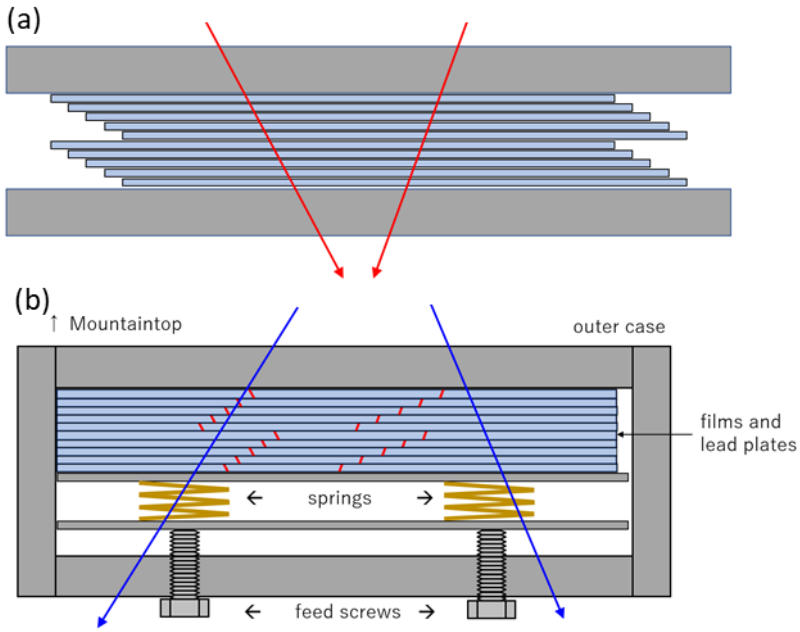

Figure. 2.3: Schematic figure of the position of the aluminum frame during transport and observation. (a) Schematic figure of the position of the aluminum frame during transport. The red line is an examples of muon tracks that passed through during transport. (b) Schematic figure of the position of the aluminum frame during observation. The bule line is an examples of muon tracks that passed through during observation. This positional relationship does not connect muon track during transport, which is represented by the red line. The film is compressed using spring during observation.

2.2.2.2. Installation Method

Observations are better done in winter since the nuclear emulsion degrades in hot and humid environments. In Mt. Omuro-yama, an event is held every February to burn the vegetation growing on the mountain. To avoid this, we performed observations from March to June. Fig. 2.4 shows scene of installation at 2019_01. We installed the detector in the following steps. Of these, the ECC azimuth and slope measurements are the parts that have been improved for the 2019 observations. The rest of the parts is similar to the 2018 observations.

Digging a hole

To avoid direct sunlight and protect the landscape, we dug a hole about 40 cm deep and buried the detector in it. To stabilize the detector, we installed a plate to put the detector on the bottom of the hole. We secured the plates and the detector with double-sided tape. To prevent rainwater entering, the boards and containers were packed in plastic bags.

Installation of the film

The film and plate with springs were put in a container. At that time, the detector began to make observations. Next, pressure was applied to the spring plate by tightening the container bolts.

Measurement azimuth and slope angle of detector

The azimuth of the detector was measured with an accuracy of 0.5° using Fiber-Optic Gyroscope (FOG) and the slope of the detector was measured with an accuracy of 1 (mrad) using a digital level. Fig. 2.5 shows the definition of detector angle. This measurement was made at installation and at retrieval. As a result, the measurements agreed within the measurement accuracy at all stations.

Azimuth and slope were also measured at retrieval to make sure that it had not moved during the observation.

Final packaging

After attaching the insulation cover to the container, the detector was buried, taking care not to move.

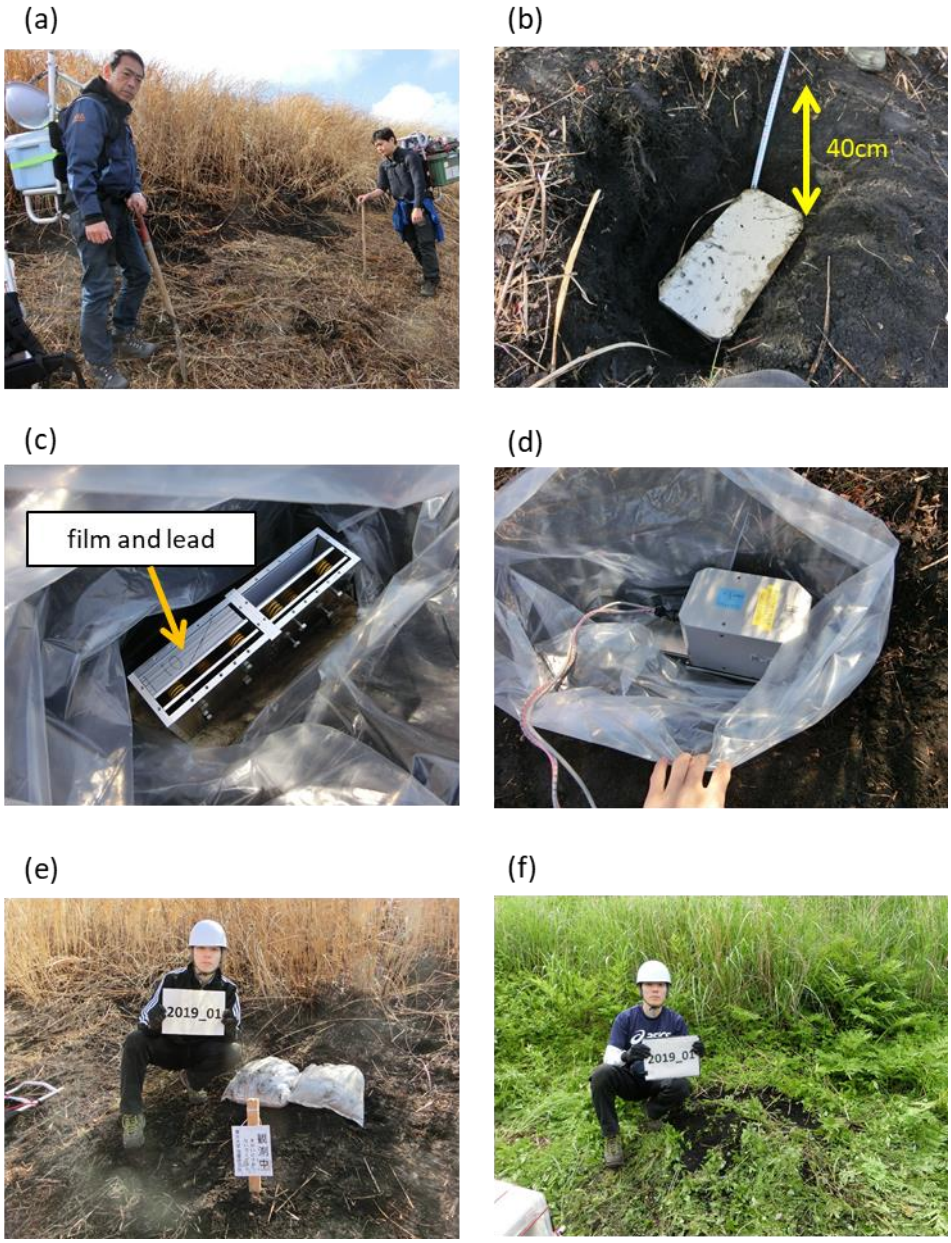

Figure 2.4: Scene of installation at 2019_01. (a) The picture before the installation. (b) Holes for installation. (c) Installing the container and the film. (d) A picture of the FOG measurement. (e) The picture before the installation (March 5, 2019). (f) The picture before the Retrieval (June 4, 2019).

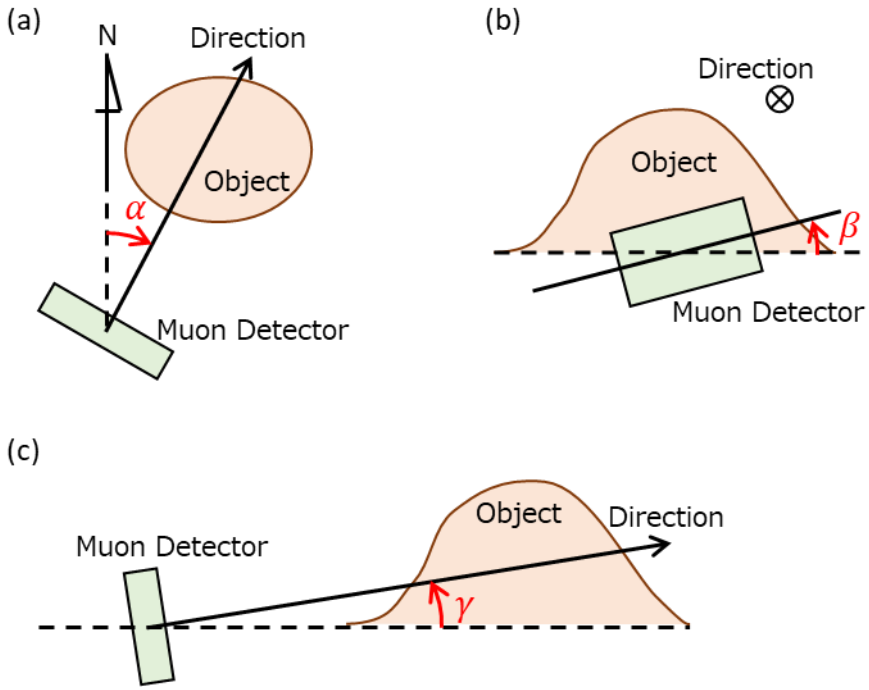

Figure 2.5: Definition of detector angle. α is a clockwise azimuth from north, β is the counterclockwise rotation angle with the azimuthal direction as the axis and γ is elevation angle of detector.

2.3. Development of multi-directional muography analysis system

In this study, we used an existing framework from film development to track reconstruction (Yoshimoto et al., 2017; Hamada et al.,2012). In this section, we describe how to select muon tracks from the reconstructed tracks and how to use the results to estimate the efficiency of the detector.

2.3.1. Track Reconstruction

The tracks recorded in the emulsion films were read using HTS (Hyper track selector) (Yoshimoto et al., 2017). The output data of the HTS is the position and orientation of the tracks recorded on the emulsion layers of both sides of the emulsion film. Track reconstruction is the process of connecting the track data of this HTS output to create a track that passes through the ECC. Track reconstruction consists of the following steps.

1) Connect the tracks recorded on both sides of the film.
2) Calculating the film-to-film alignment.
3) Connect the tracks between the films.

Track reconstruction was done using NETSCAN 2.0 (Hamada et al., 2012). NETSCAN2.0 is a framework that implements the above three steps. In this study, we used the existing framework as it is for the first two of the three steps of track reconstruction. In the third step, we adjusted the parameters to match the observed data in this study.

The first step is to connect the tracks recorded on the emulsion layers of both sides of the film. The connected tracks become the basic unit for connecting the tracks between films. This track is called the “base track”. Fig. 2.6 shows the schematic figure of base track.

The second step is to prepare for connecting the base track between the films. When the two films are parallel, the alignment between the two films is represented by the affine parameter and the distance between the films.

In the third step, we connect the base track to each other. The two base tracks are connected by the following procedure (Fig. 2.7).

1) Extend the base track to the midpoint of the two emulsion layers.
2) At the midpoint, connect the two base tracks that match within the allowable range of position and angle.

The connection relationship between base tracks is called a “linklet”. By connecting linklets, we can construct a track that penetrates the entire ECC. A “group” is a combination of base tracks connected by linklets (Fig. 2.9). A reconstructed track is one in which the track in ECC is reconstructed by the connection relationship of linklets in a group. A “chain” is a set of base tracks connected in order from upstream in a group. When there are linklet branches in a group, a single group contains multiple chains.

In making the linklet, two parameters were adjusted to match the observed data in this study.

The first is the allowable angle when connecting the base track. This allowance needs to be set separately for the radial and lateral directions because the measurement accuracy in the radial and lateral directions differs depending on the characteristics of the HTS. When this tolerance is set too wide, the possibility of two base tracks being connected from one base track increases (Fig. 2.8). On the other hand, if the tolerance is made too narrow, linklet connection failures occur. Therefore, the allowable values were initially set to a wide range for the analysis, and then narrowed down to a range that would not result in dropped connections. The final connection tolerance was set to 0.02

(rad) in the Lateral direction and $0.02 + 0.08\theta$ (rad) in the Radial direction, where $\theta = \sqrt{\tan^2\theta_X + \tan^2\theta_Z}$. Fig. 2.10 shows an example of the actual distribution of the angle difference. It was confirmed that the current angle tolerance setting is wide enough.

The second adjustment is the selection of the pair of films to make the linklet. In principle, a linklet can be made for two arbitrary films of ECC. However, when we make a linklet with two films that are far apart, the number of base tracks that enter the angle tolerance increases, resulting in more branching. In this study, we took this balance into account and created linklets to two neighboring films. Fig. 2.9 shows example of creating a linklet to two adjacent films. Since the linklet is made until two neighboring films, the chain that penetrates the ECC is the one that was connected by allowing up to one piece of film to be skipped. For example, in Fig. 2.9, the base track has not been found in PL03, but we have been able to create a chain that connects PL01 to PL07. Thus, reconstructed track includes the case where the base track is not found for some films. The hit pattern indicates in which film the base track was found. The distribution of the circles in Fig. 2.9 (b) shows the hit pattern for each chain. Since we have 20 sheets of film for the actual observation, the number of hit patterns that penetrate the ECC under the linklet creation conditions of this study is the number of cases when selecting a number from 1 to 20, allowing up to one skip. The number in this case is 17711 ways.

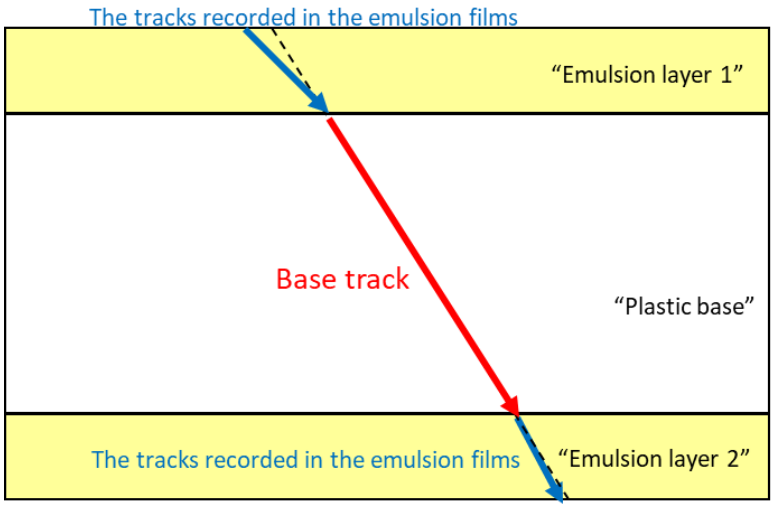

Figure 2.6: Schematic figure of Base Track making. The track is recorded on the emulsion layer on both sides of the emulsion film. The base track is the link between the tracks in the emulsion layer.

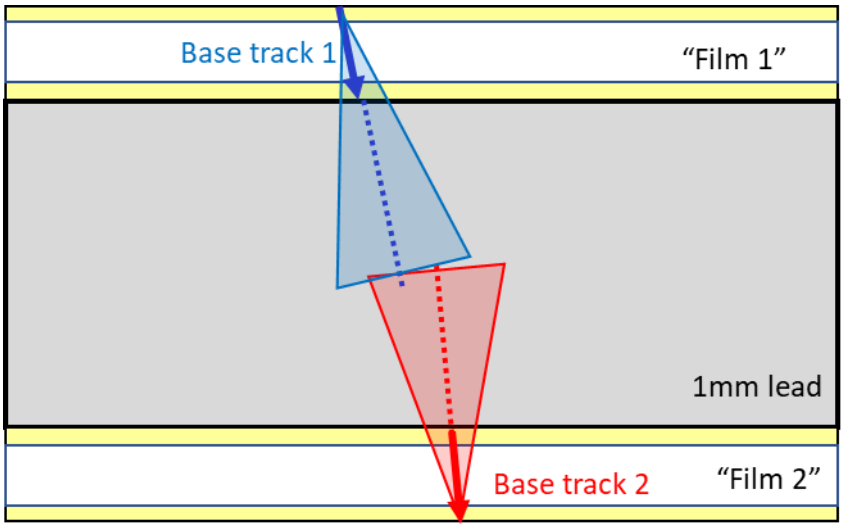

Figure 2.7: Schematic figure of linklet making. The blue triangles represent the allowable range of positions for base track 1. The red triangles represent the allowable range of positions for base track 2. Two base tracks are connected when they overlap at the midpoint of the two emulsion layers within an acceptable range of positional misalignment and if the angular misalignment of the two base tracks is within an acceptable range.

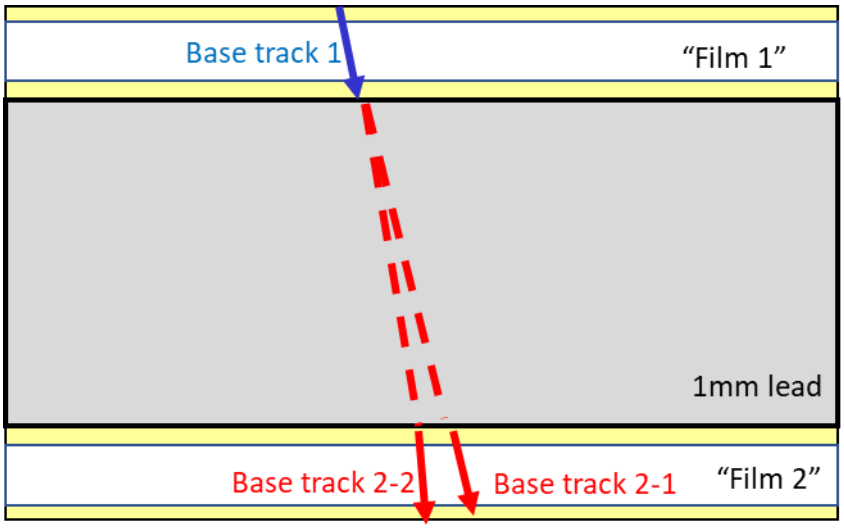

Figure 2.8: Example of linklet branching. When the position and direction of base track 2-1 and baset track 2-2 are close, base track 1 makes a linklet with both base tracks.

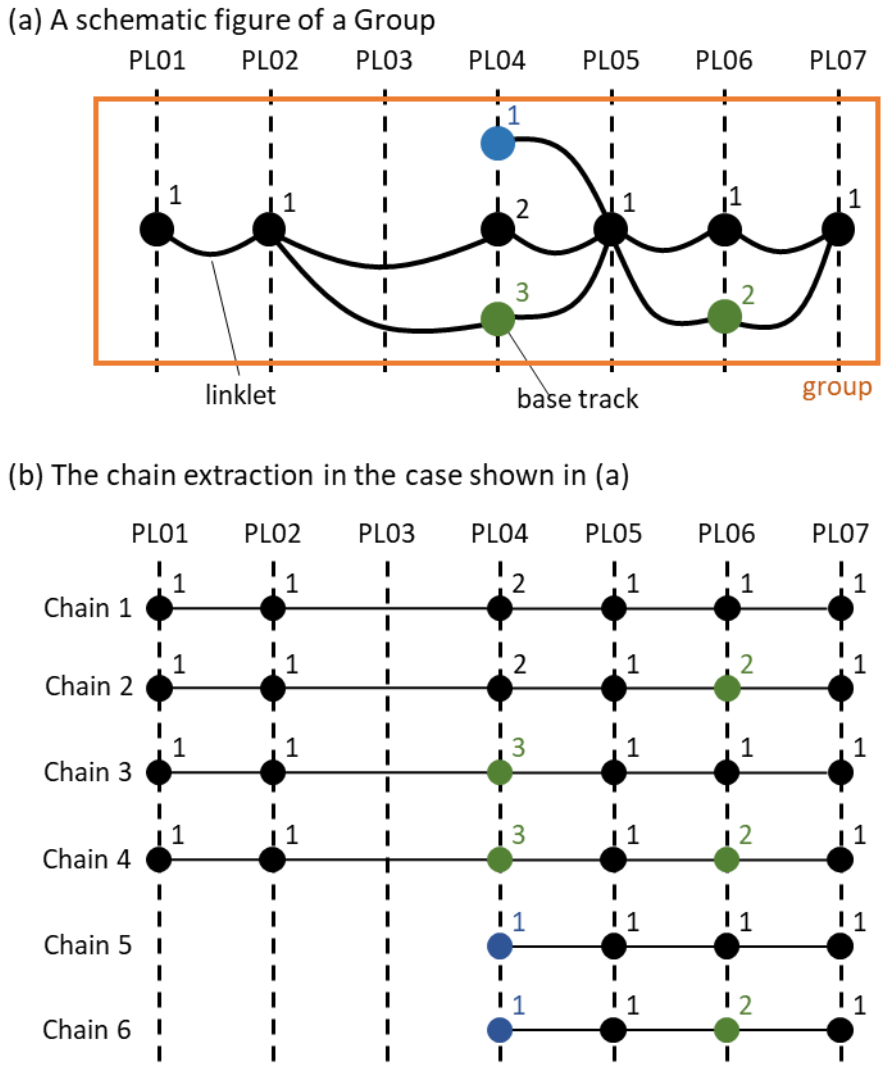

Figure 2.9: A schematic figure of a Group and Chain. (a) A schematic figure of a Group. This is an example of creating a linklet to two neighboring films. By making up to two neighboring linklets, we can connect the base tracks of PL02 and PL04 even if the base track cannot be found in PL03. (b) An example of the Chain extraction in the case shown in (a). Circles indicate hit patterns. The number indicates which base track in the same film in (a) was used.

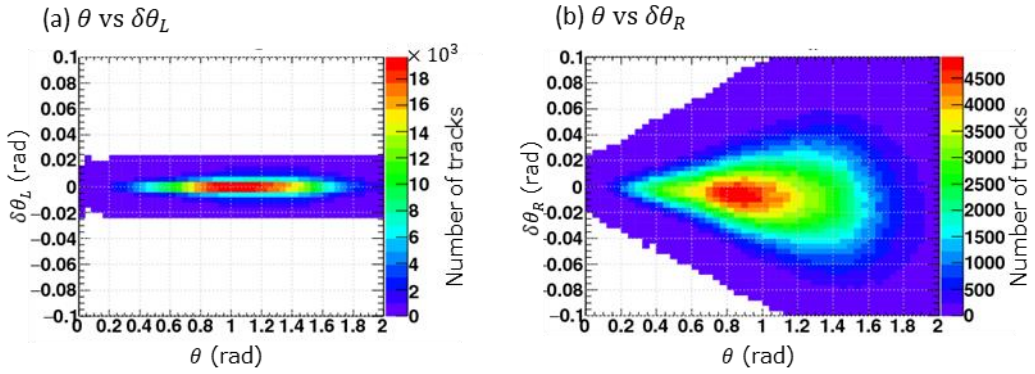

Figure 2.10: Example of the angle difference between PL01 and PL02 in ECC02. The reason for the large number of tracks at θ = 0.2 to 1.6 is that this region has a large muon flux. (a) Angular difference in Lateral direction. The horizontal axis is $\theta = \sqrt{\tan^2\theta_X + \tan^2\theta_Z}$ and the vertical axis is the angle difference between the films. (b) Angular difference in Radial direction. The horizontal axis is θ and the vertical axis is the angle difference between the films.

2.3.2. Track Selection

2.3.2.1. Selection Method

The results of track reconstruction include many signals other than muons. In this section, we describe how to select a track to be used in muography from the results of track reconstruction.

There are a number of chains in a group, depending on the branching of linklets. An example of a reconstructed track is shown in Fig.2.11. Most of the branches like case 2 are considered to be caused by a fake base track due to random noise or low-energy positrons/electrons coincidentally existing at parallel angles near the base track. These branches are eliminated by selection. For these branches, a single track is extracted by selection. On the other hand, branches such as case 3 are considered to be caused by muon tracks with similar angles nearby coincidentally.

The films forming the ECC were assigned "plate numbers" in order starting from the upstream side. For example, the most upstream (mountain side) film of ECC01 is called ECC01_PL01.

Since reconstructed tracks contain noise, a selection was applied to tracks. Selection

was made according to the following procedure.

1) Exclude those with more than 100 chains in the group.
2) Select a track that starts from one of the two most upstream (mountain side) films and stops at one of the two most downstream films.
3) If base tracks are not found in two adjacent films, the track is considered to have stopped there.
4) Evaluate the straightness using the χ^2 value.
5) Select one or two tracks from the group, depending on the branching pattern of the tracks.

The first step is to exclude processing heavy groups. Fig. 2.12 shows an example of number of chains per group. When multiple branches occur in a group, the number of chains increases by multiplication because the chains are taken in combination. While the total number of groups is more than 1,000,000, the total number of chains that are more than 100 is less than 200. Therefore, this part was excluded from the revision period as its influence on the whole is small. With this procedure, case 4 in Fig.2.11 are excluded.

The second and third steps are the conditions under which the track is considered to have penetrated the ECC. With this procedure, case 6 and case 7 in Fig. 2.11 are excluded.

The fourth step is to exclude low energy tracks by evaluating the linearity of the tracks. According to Nishiyama et al. (2016), particles with momentum less than 1 GeV/c are the source of noise in muography. The structure of the ECC, which consists of alternating layers of emulsion film and lead plates, is designed to discriminate between particles with this low momentum. The lower the momentum of the particle passing through the ECC, the larger the scattering angle on the lead plate. Therefore, by evaluating the linearity of the reconstructed track, we can estimate the momentum of the particles passing through the ECC. In this study, we used the same method as Nishiyama et al. (2014b) to evaluate the linearity of reconstructed tracks. For all possible trajectories, including branches, the value defined by the following equation was calculated to evaluate the straightness of the track.

$$\frac{\chi^2}{n} = \frac{1}{n}\sum_{i=1}^{n}\left[\left(\frac{\Delta\theta_R^i}{\sigma_R^i}\right)^2 + \left(\frac{\Delta\theta_L^i}{\sigma_L^i}\right)^2\right], \qquad (2-1)$$

where $\Delta\theta_R^i(\mathrm{rad}) = (\Delta\theta_X^i \times \tan\theta_X + \Delta\theta_Z^i \times \tan\theta_Z)/\theta$, $\theta = \sqrt{\tan^2\theta_X + \tan^2\theta_Z}$,

$\Delta\theta_L^i = (\Delta\theta_Z^i \times \tan\theta_X - \Delta\theta_X^i \times \tan\theta_Z)/\theta$, $\Delta\theta_X^i$ and $\Delta\theta_Z^i$ are angular differences along the coordinate X, Z of the ECC between a possible adjacent film pair i in a track, θ_X and θ_Z (rad) are angular along the coordinate X, Z. σ_R^i and σ_L^i are the angular measurement errors in radial and lateral components. This value was obtained by selecting a reconstructed track with particularly good linearity and taking the variance of the angular difference of the base track from which the linklet was made. Fig. 2.13 shows an example of σ_R^i and σ_L^i. In this ECC, since there are 20 films, the maximum value of n is 19.

The relationship between the linearity of the reconstructed track and the momentum of the particles depends on the structure of the ECC. Therefore, the method of selecting the track also depends on the shape of the ECC. In this study, we selected a track that satisfies $\chi^2/n < 5.0$. We will discuss whether this threshold is sufficient to cut energy in section 2.3.1.2. With this procedure, case 5 in Fig. 2.11 are excluded.

The last step is to deal with the case where tracks of the same direction happen to exist in the same location.

A) If the shared proportion of base track length is 20% or more, choose the longer branch. If the lengths are the same, choose the branch of the smaller χ^2/n.
B) If it is less than 20% (branching pattern as shown in Fig. 2.11, case4), divide into two tracks.

With this procedure, one muon track is selected for case 1 and case 2 in Fig. 2.11, and two muon tracks are selected for cases such as case 3 in Fig. 2.11.

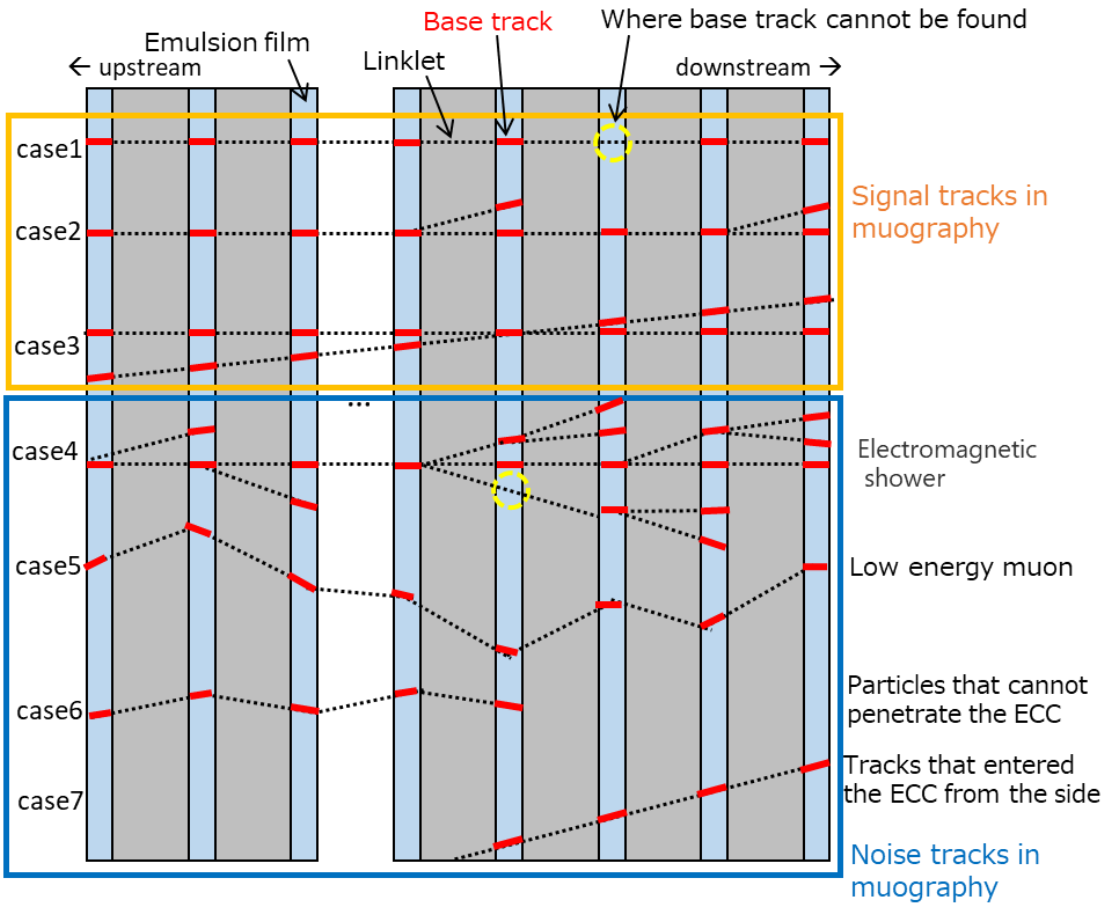

Figure 2.11: Schematic diagram of a typical example of reconstructed tracks. The light blue area represents the emulsion film. The red line represents the base track. The black dotted line represents the linklet that connects the base tracks. The linklet was created up to between the two films away. The yellow circle represents the case where a linklet is created between the base track of two neighboring films and no base track is found in the intervening film. The reconstruction tracks are grouped by those that use the same base track. The following case 1 to case 7 are examples of grouped reconstructed tracks. The reconstruction tracks include not only the signal tracks in the muography (case 1, 2, 3), but also the noise tracks (case 4, 5, 6, 7). Case 1: A straight track without any branches. Case 2: A straight track with a branch at some films. Case 3: A pair of straight tracks with small closest distances and similar angles. Case 4: Example of an electromagnetic shower. Case 5: Low energy muon. Case 6: Particle that cannot penetrate ECC. Case 7: Track that entered the ECC from the side.

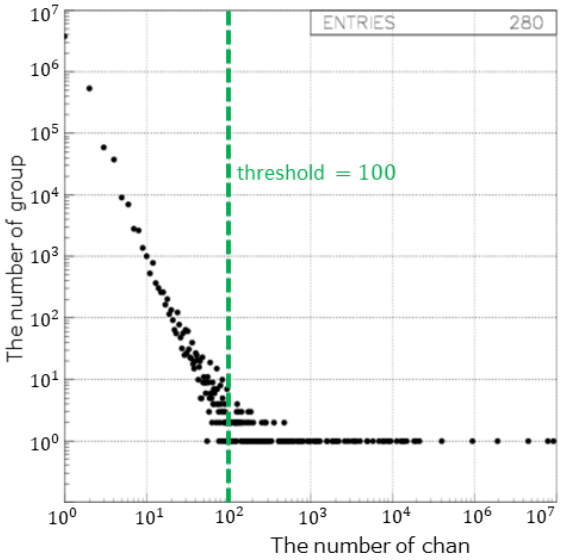

Figure 2.12: nchain distribution of ECC02 before track selection. While the total number of groups is more than 1,000,000, the total number of all the number of chains that are more than 100 is less than 200. Therefore, this part was excluded from the revision period as its impact on the total is small.

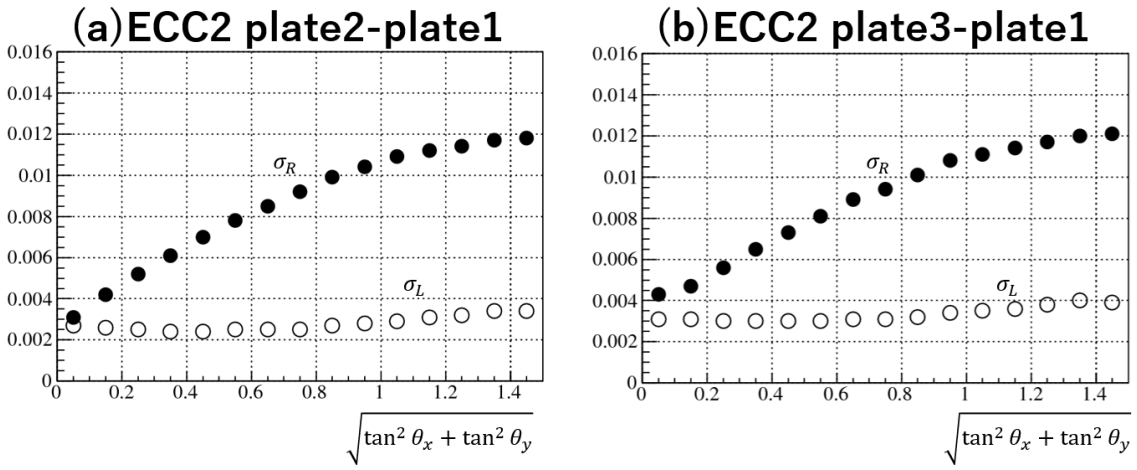

Figure 2.13: Accuracy of angle determination. The horizontal axis is $\sqrt{\tan^2\theta_X + \tan^2\theta_Z}$. The vertical axis is Accuracy of angle (rad). Black dots indicate accuracy in the radial direction, and white dots indicate accuracy in the lateral direction. Due to the characteristics of HTS, the accuracy of determining the radial direction depends on $\sqrt{\tan^2\theta_X + \tan^2\theta_Z}$. (a) Accuracy of angle determination between PL01 and PL02 (ECC02). (b) Accuracy of angle determination between PL01 and PL03 (ECC02). This value was obtained by selecting a reconstructed track with particularly good linearity and taking the variance of the angular difference of the base track from which the linklet was made.

2.3.2.2. Relationship between track selection and momentum cut

In section 2.3.2.1, we discussed how to select a track to be used for muography from reconstruction tracks. In order to simplify the selection procedure, the same selection conditions were imposed for all ECC and muon arrival directions. In this section, we discuss the suitability of this selection condition. According to Nishiyama et al. (2016), by excluding particles with momenta below 0.6 Gev/c, the flux of background noise particles is smaller than the flux of the signal assumed in the observations of this study. On the other hand, when the density length is more than 30 m.w.e. for analysis, the momentum of muon used as a signal is more than 6 Gev/c. Therefore, the threshold for selection by momentum cut should be within the range of 0.6 Gev/c to 6.0 Gev/c. In this section, we verified that the momentum thresholds corresponding to the selection conditions in the previous section fall within this range through simulation.

In this section, only the scattering angle due to Coulomb multiple scattering was considered in order to perform a simplified simulation. The scattering angle due to Coulomb multiple scattering is expressed as follows (Zyla et al., 2020);

$$\Delta\theta = \frac{13.6(\mathrm{MeV})}{\beta \cdot p}\sqrt{\frac{t}{T}}\left(1 + 0.038\ln\left(\frac{t}{T}\right)\right), \qquad (2-2)$$

where $\Delta\theta^2$(rad) is the scattering angle variance by Coulomb multiple scattering, β(/c) is the velocity of particle, p is the momentum of the particle (MeV/c), t(mm) is the thickness of the object, T(mm) the radiation length of a material. In the case of lead, $T = 5.6$mm.

The angle measurement accuracy of the track was assumed to be as follows.

- Radial direction: Linear change from 0.003 to 0.014 (rad) between $\theta = 0$ and 1.2 (rad), and constant at 0.014 (rad) above that.
- Lateral direction: Constant at 0.003 (rad).

This value of angular measurement accuracy is a linear model of the value in Fig. 2.13 obtained from actual observation data. The structure of the detector was assumed to be the same as that of the ECC.

We simulated the momentum cut using the following procedure.

1) Determine the momentum and direction of the muon.
2) Calculate the scattering angle for all 20 films in the ECC. The scattering angle is given randomly according to the angular dispersion calculated by the Coulomb multiple scattering equation.
3) Calculate the chi-square value according to Eq. (2-1).
4) Based on the chi-square value, evaluate whether this track satisfies the selection condition or not.
5) Repeat steps 1 to 4 10000 times for muons of the same momentum and direction, and obtain the ratio of tracks that satisfy the selection condition (surviving rate).
6) Repeat steps 1 to 5 for different momentum, and set the momentum at which the surviving rate exceeds 0.5 as the threshold for cutting.

Muon momentum was assumed to be from 0.01 (GeV/c) to 100 (GeV/c). There are two reasons for a different arrival direction. First, the effective thickness of the muon penetrating the lead plate in the ECC becomes thicker when the muon is incident a

direction. Second, the angle determination accuracy used in track selection depends on the angle.

Fig. 2.14 shows the distribution of χ^2/n for $X = 0\text{rad}$ and $Z = 0\text{rad}$. As the momentum increases, the distribution of χ^2/n moves to the left. Fig. 2.15 shows an example of the surviving rate. Since the surviving rate changes rapidly, which surviving rate value is taken as the threshold for momentum cut has little effect on the momentum cut value. Fig. 2.16 shows the momentum cut for each direction of arrival of the muon. The value of momentum cut became larger as the angle increased. This is because the effective thickness of the penetrating lead plate is larger. For all directions of arrival, the momentum cut values fall within the range of 0.8 Gev/c to 2.6 Gev/c. Therefore, the current selection conditions were found to be appropriate for all arrival directions.

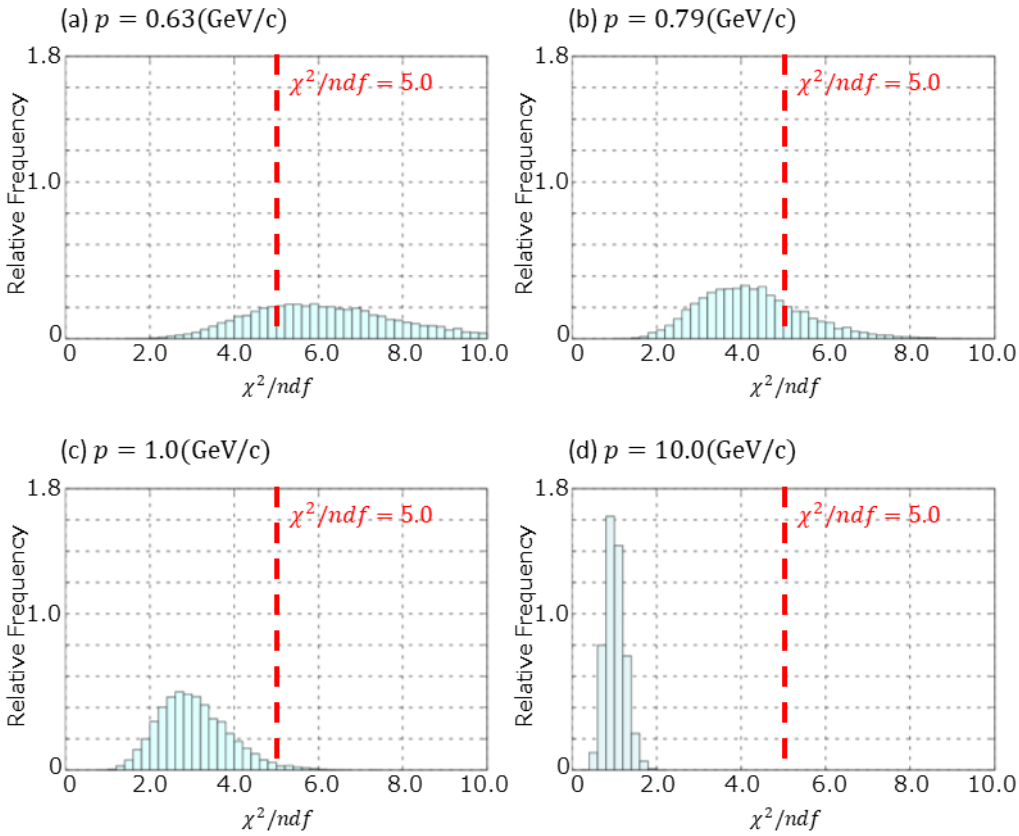

Figure 2.14: The distribution of χ^2/ndf for $X = 0\text{rad}$ and $Z = 0\text{rad}$. The red line is the threshold for selection. The percentage of tracks included to the left of this line is the surviving rate. (a) The momentum of muon is 0.63(GeV/c). (b) The momentum of muon is 0.79(GeV/c). (c) The momentum of muon is 1.0(GeV/c). (d) The momentum of muon is 10.0(GeV/c).

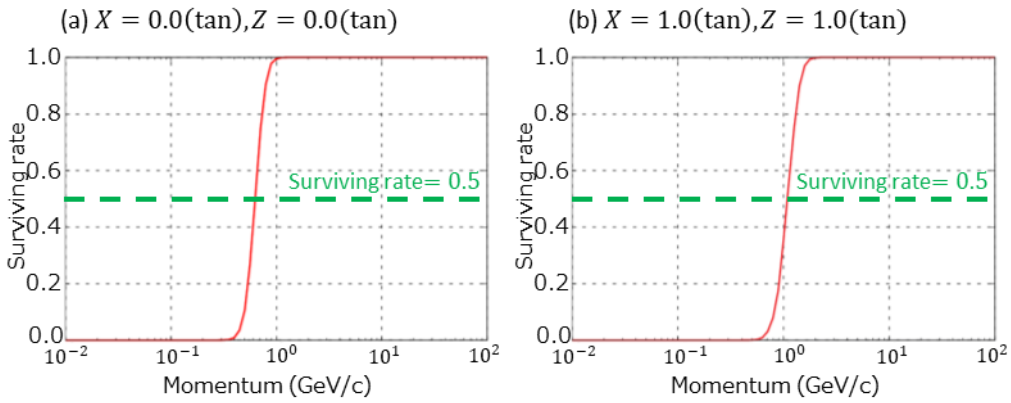

Figure 2.15: An example of the surviving rate. The green line is the threshold for momentum cut. The momentum at which the surviving rate exceeds this line is the value of the momentum cut. (a) $X = 0$rad and $Z = 0$rad. (b) $X = 1.0$rad and $Z = 1.0$rad.

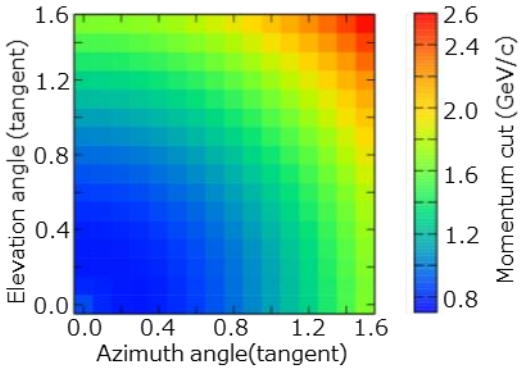

Figure 2.16: the momentum cut for each direction of arrival of the muon.

2.3.3. Efficiency estimation

Not all muons that penetrate the ECC are detected as reconstruction tracks. Muons may not be detected for several reasons. The possible causes are as follows.

1) Limitations of HTS Track Recognition.
2) Inefficiencies when creating base tracks in NETSCAN 2.0.
3) Inefficiencies when creating linklets in NETSCAN 2.0.

What we need is the percentage of the muons that penetrated the ECC that are included in the selected reconstruction track. This ratio is called "efficiency". It is difficult to evaluate these effects one by one due to the complexity of the task. Therefore, here we

have developed a method to estimate the efficiency of each film from the selected reconstruction tracks. The efficiency of each film was used to determine the overall efficiency of ECC.

In order to estimate the efficiency of a film, it is necessary to have tracks that have been detected and tracks that have not been detected on that film. A hit pattern is a representation of whether or not a track remains on the film. When there are three consecutive films, even if the base track cannot be found on the middle one, the base tracks of the first and third films that are connected are included in the selected reconstruction track. Figure 2.17 shows an example of a hit pattern from the fourth (PL04) to the sixth (PL06) film in the ECC. Consider the case of determining the efficiency of the PL05 film. Fig. 2.17 (a) to (h) all assume that the muon actually penetrates the ECC. During track selection, when the base track is not found for two or more consecutive films, a linklet is not created, so all cases (g) and (h) are not included in the track selection results. (c) to (e) may or may not be included in the track selection depending on whether the base track is found in the neighboring PL03 or PL07. Therefore, only (a) and (b) are certainly included in the track selection. We used (a) and (b) in our calculations because the tracks used to calculate the efficiency of PL05 must all be included in the results of track selection, regardless of whether or not a base track is found in PL05. When the number of tracks corresponding to the two hit patterns in the red box are N_a and N_b, the efficiency of PL05 ϵ_5 can be expressed as follows:

$$\epsilon_5 = \frac{N_a}{N_a + N_b}. \qquad (2-3)$$

Using the efficiency of a single film, the efficiency ε of ECC can be obtained as follows:

$$\bar{\epsilon_i} = 1 - \epsilon_i$$

$$\varepsilon = (\epsilon_1 \times \epsilon_2 \times \ldots \times \epsilon_{20}) + (\epsilon_1 \times \bar{\epsilon_2} \times \ldots \times \epsilon_{20}) + \cdots + (\epsilon_1 \times \epsilon_2 \times \ldots \times \bar{\epsilon_{20}}). \qquad (2-4)$$

The sum of the right-hand side is taken for all the hit patterns that correspond to the track selection, for example, $\epsilon_1 \times \bar{\epsilon_2} \times \epsilon_3 \times \ldots \times \bar{\epsilon_{18}} \times \epsilon_{19} \times \epsilon_{20}$ or $\bar{\epsilon_1} \times \epsilon_2 \times \epsilon_3 \times \ldots \times \epsilon_{18} \times \bar{\epsilon_{19}} \times \epsilon_{20}$ with the track selection condition. The hit pattern is two independent choices for all 20 layers of film, so the total number of patterns is 2^{20}. The number of hit patterns that penetrate the ECC under the linklet creation conditions of this study is the number of cases when selecting a number from 1 to 20, allowing up to

one skip. The number in this case is 17711 ways. Since the overall efficiency of the ECC is the sum of these 17711 ways, the overall detection efficiency of the ECC can be higher than the efficiency of each film.

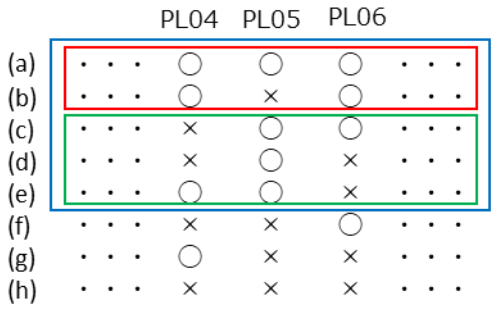

Figure 2.17: Example of a hit pattern from the fourth to the sixth page in the ECC. The number of tracks in the hit pattern (a) is N_a. The blue frame shows the hit pattern used in track selection. The red frame is the hit pattern used to find the efficiency of PL05. The green frame is strictly based on the hit pattern of PL03 and PL07, which may or may not be used in track selection. The two hit patterns in the red frame are not affected by PL03 or PL07 when track is selected.

2.4. 3-D density reconstruction for multi-directional muography

We improved the method of linear inversion by Nishiyama et al. (2014) for multi-directional muography. We reconstructed the 3-D density distribution applying this method to observation muon counts data. The method of Nishiyama et al. (2014) has the following points that can be improved.

1. Clarifying the treatment of areas where voxels are not defined.
2. Consideration of solid angle area of muon arrival direction.

The treatment of out of voxels

In actual observations, there may be other structures outside the area where we are interested in obtaining the density distribution. For example, we define the analysis area as above a certain elevation, there is a path length that passes near the observation point. There may also be another structure behind the object (Fig. 2.18). In these cases, we treated the contribution of that part as follows.

(a) Assign the reconstruction voxels

(b) Assuming a density length of that part

(a) is the simplest solution. This method is better when the properties of the analysis region and the added voxels are considered to be close. When the properties of the analysis region and the added voxels are considered to be different, (b) is the better method. For example, the case where the analysis region is a scoria cone with a lava dome behind it.

When there is material outside the reconstructed region, that part also contributes to the density length. In this case, equation (1-7) is written as

$$d_i = \sum_{j=1}^{J} A_{ij}\,\rho_j + d_i^{out}, \qquad (2-5)$$

where d_i^{out} is the density length outside the reconstructed region of i-th path. d_i^{out} require assumptions because this cannot be obtained from observations. In this study, the density was assumed to be constant across the i-th path.

$$d_i^{out} = \rho_i^{out} p_i^{out}, \qquad (2-6)$$

where ρ_i^{out} is the assumed density, p_i^{out} is the path length outside the reconstructed region of i-th path. ρ_i^{out} also require assumption.

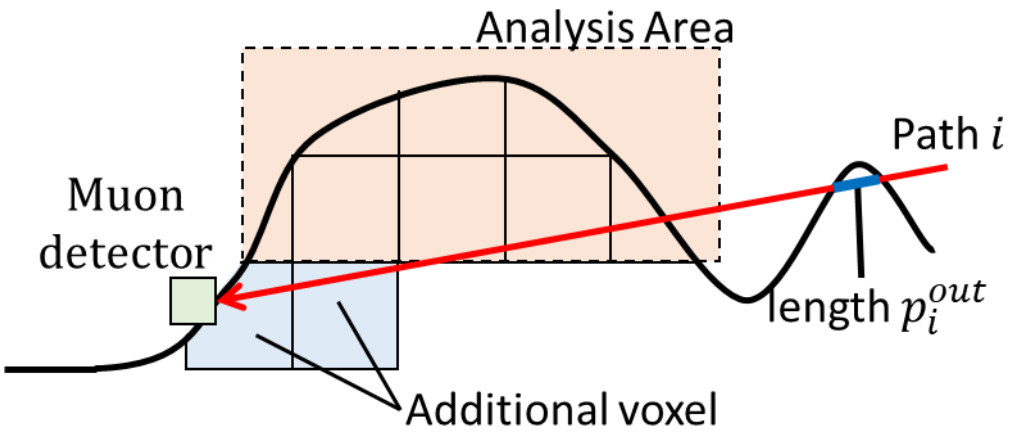

Figure 2.18: Schematic view of the path length outside the reconstructed region.

Consideration of solid angle area of muon arrival direction

The number of detected muons of i-th solid angle area N_i is the integration of the muon counts from solid angle area Ω_i (Fig. 2.19). Therefore, the voxels through the solid angle area contribute to N_i.

In Nishiyama et al. (2014), when they made the observation matrix, only the central direction of the solid angle was considered because density length was defined on a straight line.

Jourde et al. (2015) showed how the beam spread can be reflected in the 3D density reconstruction calculation. They changed the input data from density length to muon flux to define data for the solid angle area Ω_i. They used the mean of the solid angle area as the flux. They were able to ignore the differences in flux due to elevation angle. because the angular width of their telescope was small (50 mrad).

In this study, the maximum angular width is 200 mrad because of the small number of observation muons, so we should consider the elevation angle change in the solid angle area. To consider this, we improved the observation matrix. We defined the sub paths for the i-th path $(\iota_1, \iota_2, \ldots, \iota_M)$ as paths in the solid angle area Ω_i (Fig. 2.19). Then, the relationship between the j-th voxel density ρ_j and the density length of "i_ι-th" sub path can be written as follows, as in equation (2-5)

$$d_\iota = \sum_{j=1}^{J} {}^{sub}A_{i_\iota j}\,\rho_j + \rho_{i_\iota}^{out} p_{i_\iota}^{out}, \qquad (2-7)$$

where ${}^{sub}A_{i_\iota j}$ is the length of the "i_ι-th" path across the j-th voxel. "sub" represents that it is an observation matrix for the sub path divided in the solid angle. To define data for the solid angle area Ω_i, we changed the input data from density length to muon counts to define data for the solid angle area Ω_i as well as Jourde et al. (2015). Muon counts are not linearly related to density length. However, for small density length fluctuations, we assume that muon counts are approximated by a first-order expansion around the local density length $d_{i_\iota}^0$. $d_{i_\iota}^0$ is the density length when the prior density model is $\boldsymbol{\rho_0}$. From eq. (1-3), N_{i_ι} can be written as

$$N_{i_\iota} = N_{i_\iota}^0 + \delta N_{i_\iota} \approx f_{i_\iota}^{-1}\left(d_{i_\iota}^0\right) + \left(d_{i_\iota} - d_{i_\iota}^0\right)\frac{\partial f_{i_\iota}^{-1}}{\partial d_{i_\iota}}\left(d_{i_\iota}^0\right), \qquad (2-8)$$

where $N_{i_\iota}^0$ is the muon counts when the density length is $d_{i_\iota}^0$. From eq. (2-8) and eq. (2-7),

$$\delta N_{i_\iota} \approx \left(\left(\sum_{j=1}^{J} {}^{sub}A_{i_\iota j}\,\rho_j + \rho_{i_\iota}^{out} p_{i_\iota}^{out}\right) - \left(\sum_{j=1}^{J} {}^{sub}A_{i_\iota j}\,\rho_j^0 + \rho_{i_\iota}^{out} p_{i_\iota}^{out}\right)\right)\frac{\partial f_{i_\iota}^{-1}}{\partial d_{i_\iota}}\left(d_{i_\iota}^0\right)$$

$$\delta N_{i_\iota} \approx \sum_{j=1}^{J} \frac{\partial f_{i_\iota}^{-1}}{\partial d_{i_\iota}}\left(d_{i_\iota}^0\right) {}^{sub}A_{i_\iota j}\left(\rho_j - \rho_j^0\right). \qquad (2-9)$$

The observation matrix for muon counts ${}^{sub}A_{i_\iota j}^N$ is defined below,

$${}^{sub}A_{i_\iota j}^N = \frac{\partial f_{i_\iota}^{-1}}{\partial d_{i_\iota}}\left(d_{i_\iota}^0\right) {}^{sub}A_{i_\iota j}, \qquad (2-10)$$

where the subscript N in the upper right corner is added to explicitly indicate that it is the observation matrix for the muon number.

The muon counts of i-th solid angle area N_i is the sum of N_{i_ι} for index ι. In addition, Fig. 1.1 shows that the relation between muon flux and density length is expressed in semi-logarithmic scale, so it is better to make the observation matrix for log(N), which is less affected by the linearization. Since the derivative of a logarithm is the reciprocal, the observation matrix for $\log N_i$ can be written as follows,

$$A_{ij}^N = \sum_{\iota=1}^{\iota_M} {}^{sub}A_{i_\iota j}/N_i\,, \qquad (2-11)$$

In this case, data covariance matrix in $\log N_i$ is

$$\mathbf{C_N}(i_1, i_2) = \begin{cases} \sigma^2_{\log N_i} \ (i_1 = i_2 = i) \\ 0 \ (i_1 \neq i_2) \end{cases}, \qquad (2-12)$$

where $\sigma_{\log N_i}$ is the error of $\log N_i$ of i-th solid angle area.

From the above, the formula for 3D density reconstruction is

$$\boldsymbol{\rho'} = \boldsymbol{\rho_0} + \left({}^t\mathbf{A^N}\mathbf{C_N^{-1}}\mathbf{A^N} + \mathbf{C_\rho^{-1}} \right)^{-1} {}^t\mathbf{A^N}\mathbf{C_N^{-1}}(\log \boldsymbol{N_{Obs}} - \log \boldsymbol{N^0}). \qquad (2-13)$$

and

$$\mathbf{C_{\rho'}} = \left({}^t\mathbf{A^N}\mathbf{C_N^{-1}}\mathbf{A^N} + \mathbf{C_\rho^{-1}} \right)^{-1}. \qquad (2-14)$$

Fig. 2.20 shows a comparison between the case reconstructed using the observation matrix in Eq. 1-7 and the case reconstructed using the observation matrix in Eq. 2-11 for the same muon count simulation data. The reconstruction results are clearer when using the observation matrix of Eq. 2-11 than when using the observation matrix of Eq. 1-7.

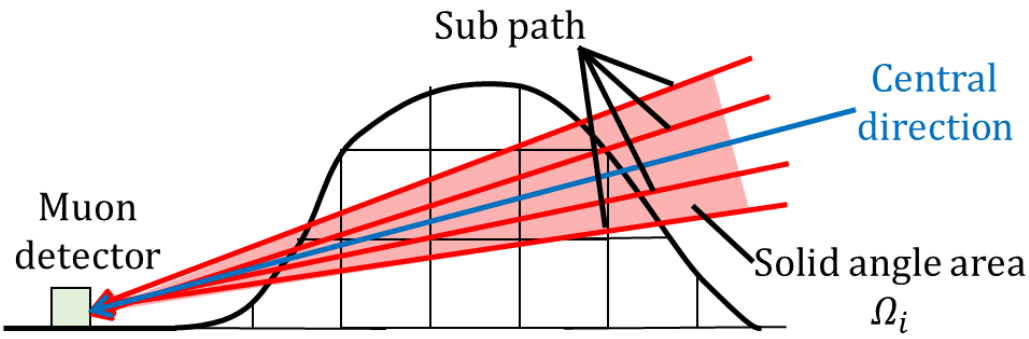

Figure 2.19: Schematic view of the solid angle area. Red area is the solid angle area. Blue line is the central direction in solid angle area. Red lines are sub paths in solid angle area.

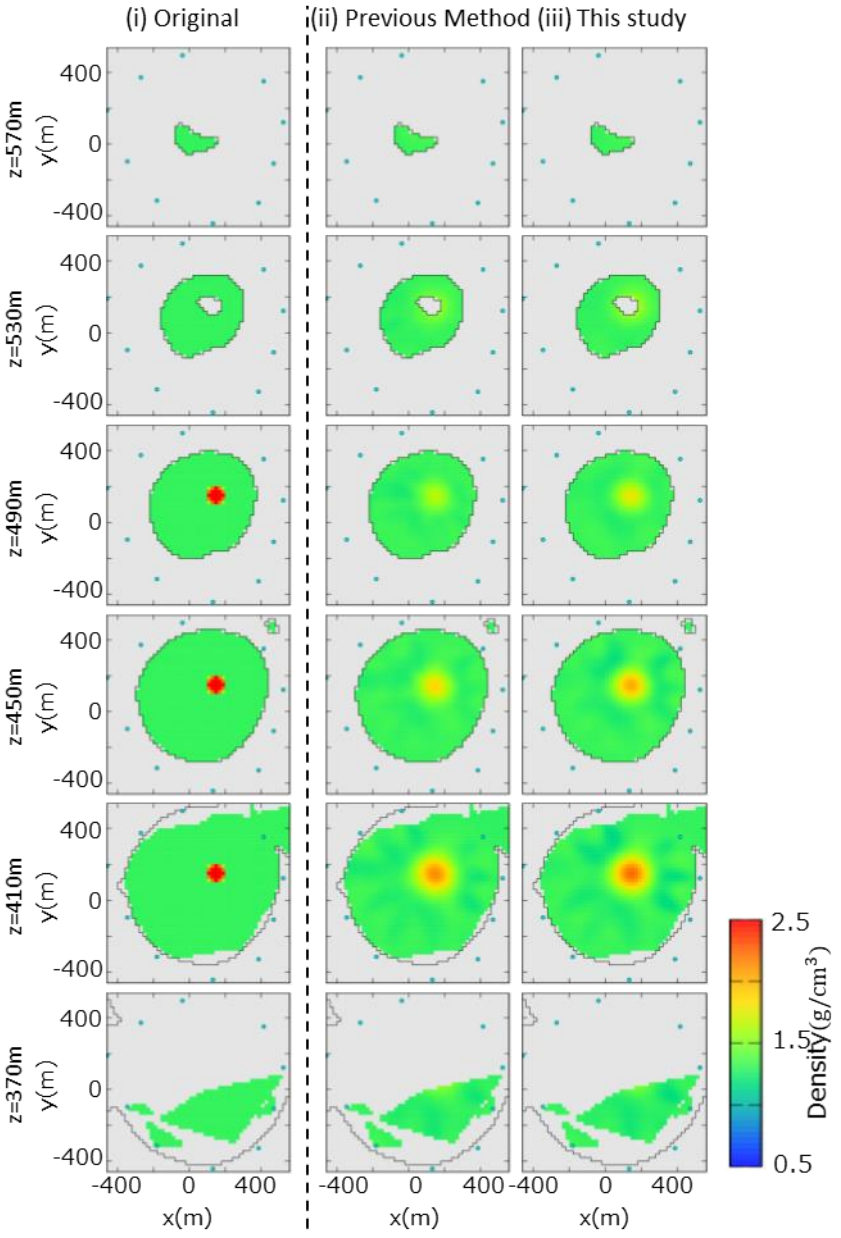

Figure 2.20: a comparison between the case reconstructed using the observation matrix in Eq. 1-7 and the case reconstructed using the observation matrix in Eq. 2-11 for the same muon count simulation data. (i) Assumed density structure. The structure is assumed to be a cylindrical structure with a diameter of 100 m and a density of 2.5 (g/cm^3) just below the crater of a mountain body with a density of 1.3 (g/cm^3). (ii) Reconstruction results using the observation matrix in Eq. 1-7. (iii) Reconstruction results using the observation matrix in Eq. 2-11.

3. Observation at Mt. Omuro-yama

3.1. Overview of observation

In 2018 observation, we installed 3 ECC around the Mt. Omuro-yama on 29–30 March 2018 and retrieved them on 1–2 June 2018. In 2019 observation, we installed 8 points around the Mt. Omuro-yama on 5–9 March 2019 and retrieved them on 3–6 June 2019. In this observation, two ECCs were installed at each observation point. Fig. 3.1 shows the position of detectors. Table 3.1 shows the information of muography stations.

Table 3.1: Description of muography stations. The coordinate origin is the summit of Mt. Omuro-yama (Latitude 34° 54′ 11", Longitude 139° 5′ 40").

Site	x (m)	y (m)	z (m)	α (deg)	β (deg)	γ (deg)	Exposure Period (days)	Effective area (m^2)
2018_A	386.4	-327.9	335.6	-31.8	0.0	0.0	64	0.0064
2018_B	-468.2	188.9	372.3	110.0	0.0	0.0	62	0.0068
2018_C	238.1	498.6	402.5	202.0	0.0	0.0	62	0.0080
2019_01	-38.8	496.4	396.9	168.0	2.0	-1.5	91	0.0150
2019_02	-270.1	373.4	378.0	135.0	1.2	-0.5	89	0.0150
2019_03	-345.9	-96.1	374.6	54.6	-1.2	-0.8	89	0.0150
2019_04	-181.0	-314.8	369.4	31.3	0.0	1.6	92	0.0150
2019_05	132.1	-442.2	339.4	343.9	0.4	-0.6	90	0.0150
2019_06	470.3	-108.2	376.0	299.9	1.2	-0.5	89	0.0150
2019_07	524.3	122.7	382.7	283.9	-1.3	-0.9	89	0.0150
2019_08	415.1	352.1	415.9	238.8	1.2	-0.1	89	0.0150

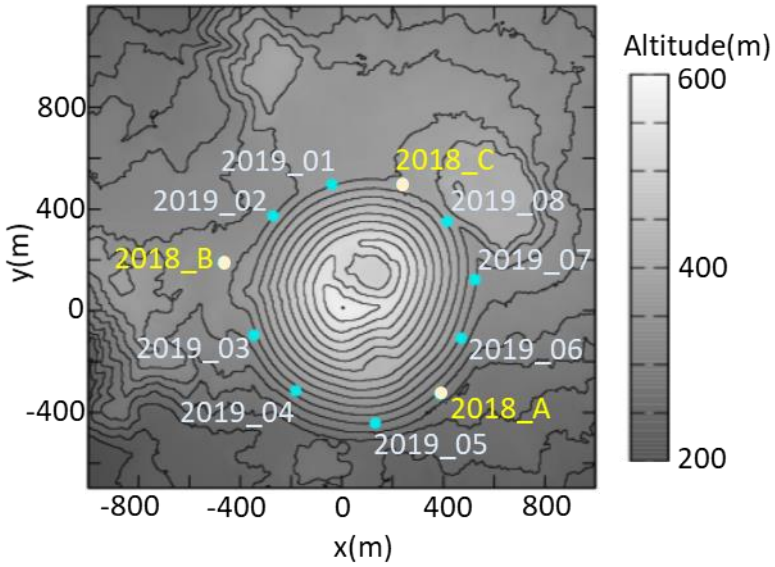

Figure 3.1: Elevation map of the Mt. Omuro-yama region and position of muon detector (blue point). The coordinate origin is the summit of Mt. Omuro-yama (Latitude 34° 54′ 11", Longitude 139° 5′ 40"). In this study, East-West coordinate is defined as x, South-North coordinate is defined as x and altitude is defined as z. Yellow dots are observation points in 2018. Blue dots are the observation points in 2019.

3.2. Track analysis of observation data

In this section, we describe the process of obtaining the observed muon counts from the observed emulsion films.

3.2.1. Developing and Scanning

All the emulsion films (320 sheets) were developed in F-lab, Nagoya University on 26-28 June 2019. Development was successful in 319 out of 320 films. Since the vacuum pack of the failed film was torn at the time of the retrieval and the ECC01 was filled with water, the cause was considered to be flooding or exposure of the film.

After the films were developed, the tracks recorded in the emulsion films were read using HTS (Hyper track selector) (Yoshimoto et al., 2017) in July-September 2019. Since each film was in a different state, the HTS settings were adjusted one by one. Specifically, we adjusted the sensitivity of the camera and the threshold of track recognition.

We scanned successfully 319 films.

3.2.2. Track reconstruction

We used NETSCAN2.0 to reconstruct the tracks (Hamada et al.,2012). The following procedure was used to reconstruct the tracks. We used the method described in section 2.3.1 to reconstruct tracks from base tracks.

Fig. 3.2 shows an example of the position distribution of the base track on the film. The number of base tracks tended to be smaller at the edges of the film. This is because the edges of the film may not scan well. Therefore, to avoid the influence of this edge, the area with a black border was used as the analysis area.

3.2.3. Track Selection

We used the method described in section 2.3.2 to select tracks from reconstructed tracks. Fig. 3.3 shows an example of the angular distribution of selected tracks in ECC02.

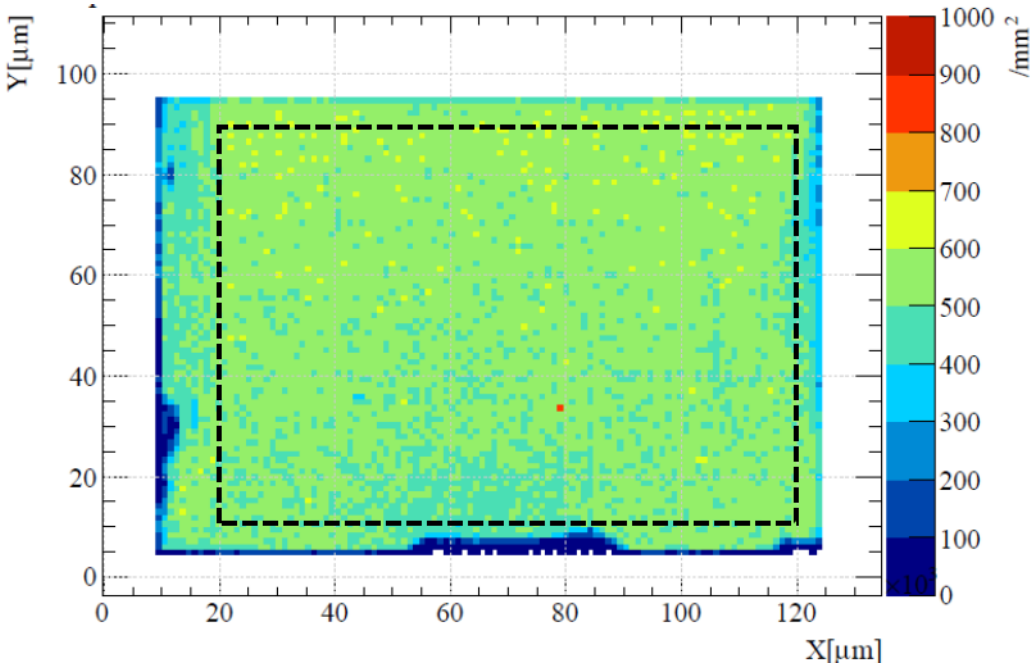

Figure 3.2: Distribution of the number of tracks on the film at ECC02-PL01. The color represents the number of base tracks per mm^2. The area with a black border was used as the analysis area.

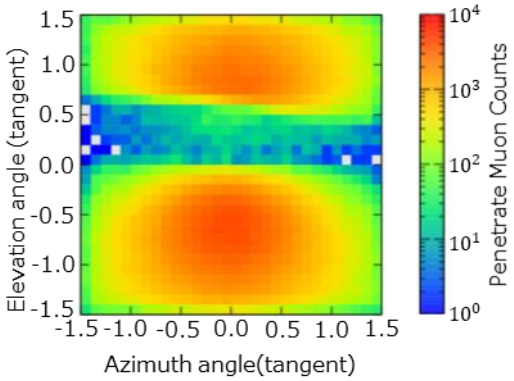

Figure 3.3: An example of the angular distribution of selected tracks in ECC02.

3.2.4. Efficiency Estimation

We used the method described in section 2.3.2 to calculate the films and detectors efficiency. Fig. 3.4 shows the example of the angular distribution of efficiency in ECC02. Where the muon flux is low (elevation angle Z = 0.0 to 0.5 (tangent)), there is variation in efficiency due to small muon counts. On the other hand, the region with Z = -0.5 to 0.0 (tangent) has large muon counts due to the absence of objects, and the variation is small. There was a tendency for point symmetry, with azimuth angle and elevation angle 0 (rad) being the point of symmetry. The characteristic non-circular shape of the high efficiency region is probably caused by the characteristics of HTS. However, the detailed cause is not clear.

When there are no muons in the direction, it is not possible to calculate efficiency. In the part through the mountain, the muon number is small, so the efficiency is not calculated in some parts. Therefore, using the point symmetry, the region with positive elevation angle was folded with the value of the region with negative elevation angle. The collapsed values are shown in Fig. 3.5.

When the absolute values of the azimuth and elevation angles were greater than 1.3 (tangent), the efficiency was lower. Therefore, in the subsequent analysis, the region with an angle of 1.3 (tangent) or less was selected for analysis.

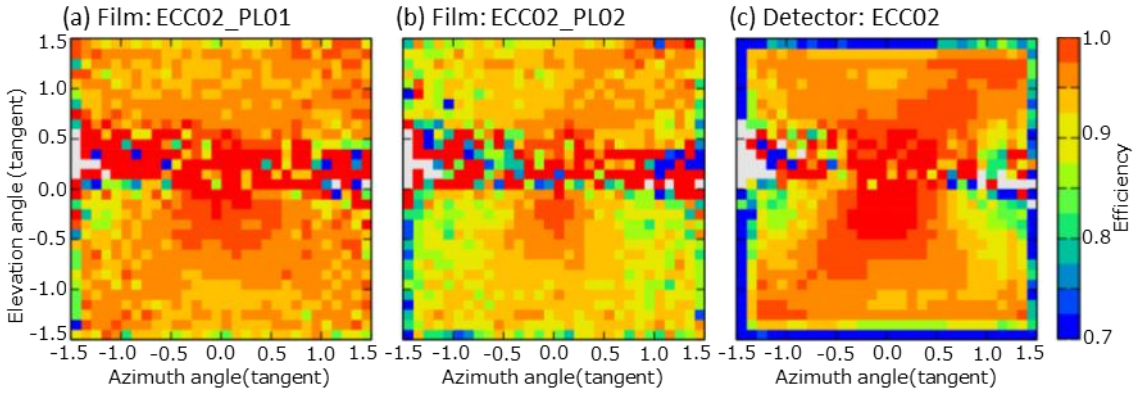

Figure 3.4: The example of the angular distribution of efficiency in ECC02. When there are no muons in the direction, it is left blank. (a) Efficiency distribution of film ECC02_PL01. (b) Efficiency distribution of film ECC02_PL02. (c) Efficiency distribution of detector ECC02 calculated from hit patterns.

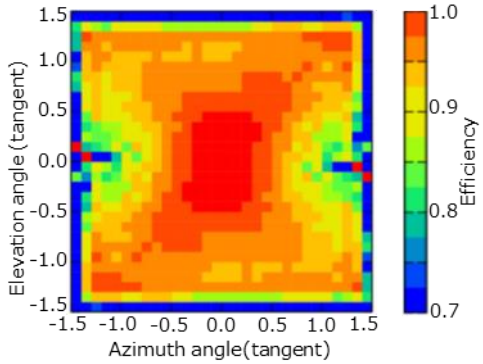

Figure 3.5: The efficiency distribution of ecc02 inverted by the value on the backward side. When the absolute values of the azimuth and elevation angles were greater than 1.3 (tangent), the efficiency was lower. Therefore, in the subsequent analysis, the region with an angle of 1.3 (tangent) or less was selected for analysis.

3.3. Calibration by comparison with Free Sky

In order to check whether there is any problem with the observed muon counts, the muon counts in the direction not penetrating the object (Free Sky area) were compared with the simulation. The detection efficiency was calibrated based on the comparison with the simulation. The muon count for the simulation is the value for density length = 0 in Fig. 1.1.

Fig. 3.6 (a) shows the ratio of the observed muon number to the simulated muon number in the free sky part of ECC02. The observed muon counts were about 80% to 100% of the simulations. In order to calibrate this deviation, a histogram of the ratio of observed to simulated muon numbers per angle bin was created (Fig. 3.6 (b)). It was calibrated using the average of the ratio of the observed and simulated muon counts. The variance was also used as the calibration error. Fig. 3.6 (c) shows the ratio of the observed muon number to the simulated muon number in the free sky part of ECC02 after calibration and Fig. 3.6 (d) shows histogram of the ratio of observed to simulated muon counts after calibration. Table 3.2 shows the calibration values and their errors for each ECC. Only ECC_C had an outstandingly large error, so it was excluded from subsequent analyses.

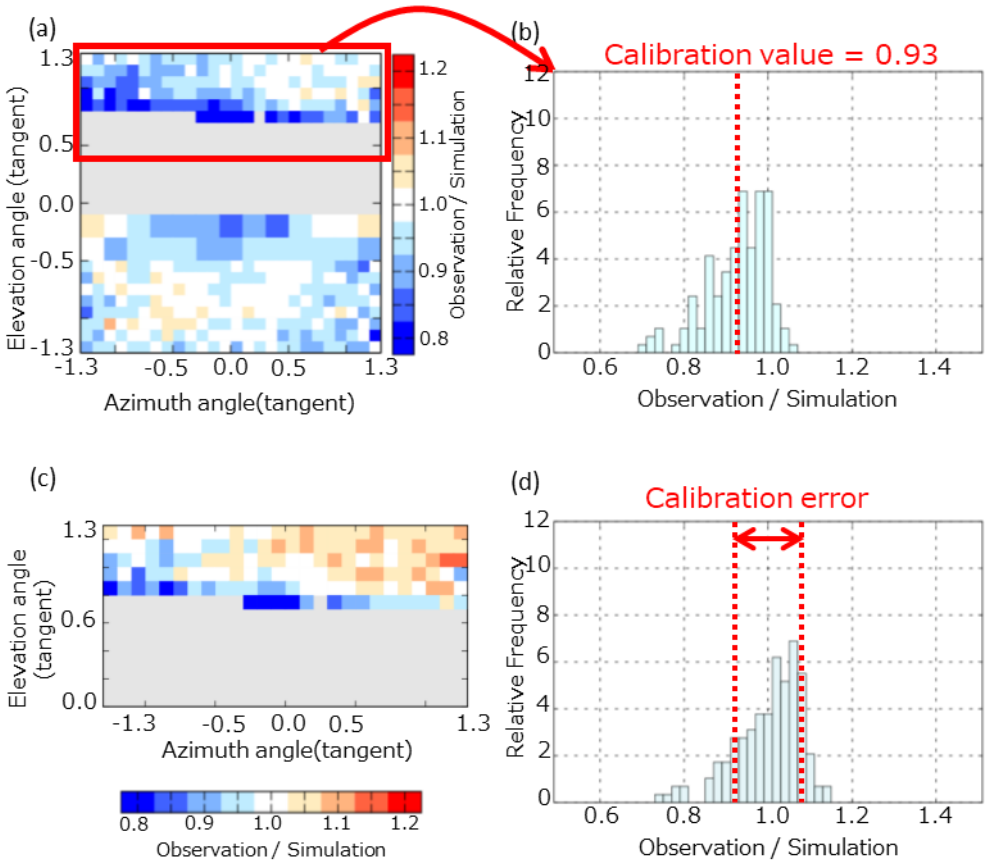

Figure 3.6: The ratio of the observed muon number to the simulated muon number in the free sky part of ECC02. (a) Ratio of observed to simulated muon counts at free sky for each angle. (b) Histogram of the ratio of observed to simulated muon counts in red square of (a). The calibration value is the average value of this histogram. (c) The ratio of the observed muon number to the simulated muon number in the free sky part of ECC02 after calibration. (d) Histogram of the ratio of observed to simulated muon counts after calibration in (c). (d) has the same distribution as (b), only the absolute value has changed. The calibration error was defined as the deviation of this histogram.

Table 3.2: Calibration values and their errors for each ECC.

ECC	Site	Calibration value	Calibration error
ECC_A	2018_A	0.83	0.19
ECC_B	2018_B	0.88	0.08
ECC_C	2018_C	0.67	0.33
ECC_01	2019_01	0.89	0.09
ECC_02	2019_01	0.93	0.08
ECC_03	2019_02	0.90	0.06
ECC_04	2019_02	0.88	0.05
ECC_05	2019_03	0.84	0.10
ECC_06	2019_03	0.79	0.09
ECC_07	2019_04	0.81	0.08
ECC_08	2019_04	0.80	0.07
ECC_09	2019_05	0.79	0.08
ECC_10	2019_05	0.87	0.07
ECC_11	2019_06	0.90	0.07
ECC_12	2019_06	0.90	0.07
ECC_13	2019_07	0.97	0.06
ECC_14	2019_07	0.96	0.07
ECC_15	2019_08	0.92	0.06
ECC_16	2019_08	0.94	0.06

3.4. Muography results for each observation point

The calibration calculated in section 3.3 was applied to the observed muon count, and the muographic results were obtained using the method described in section 1.2.2. The solid angle area Ω_i was determined by the following procedure.

1. When the elevation angle is between 0.1 and 0.5 (tangent), both the horizontal angle and elevation angle are separated by 0.2 (tangent). When the elevation angle is 0.5 (tangent) or more, both the horizontal angle and elevation angle are separated by 0.1 (tangent).
2. When the muon count in a bin is less than 24, it is combined with the surrounding

bins so that the muon count is 25 or more.

The calculation of the conversion from muon counts to mean density was done using Eq.(1-5). A numerical table of observed muon counts for mean densities from 0.5 to 3.0 (g/cm3) was created by simulation. The bins whose observed muon counts were outside the range of the numerical table were excluded from the calculation results of the average density.

Fig. 3.7 shows the results of muography. The bulk density of the mountain, calculated using all the observed data, was $1.39 \pm 0.01(\mathrm{g/cm^3})$. From only one muographic image, we could not obtain enough density distribution to interpret the specific internal structure of Mt. Omuro-yama. However, by using the muographic images of 10 points, we were able to obtain the 3-D density distribution shown in the next section.

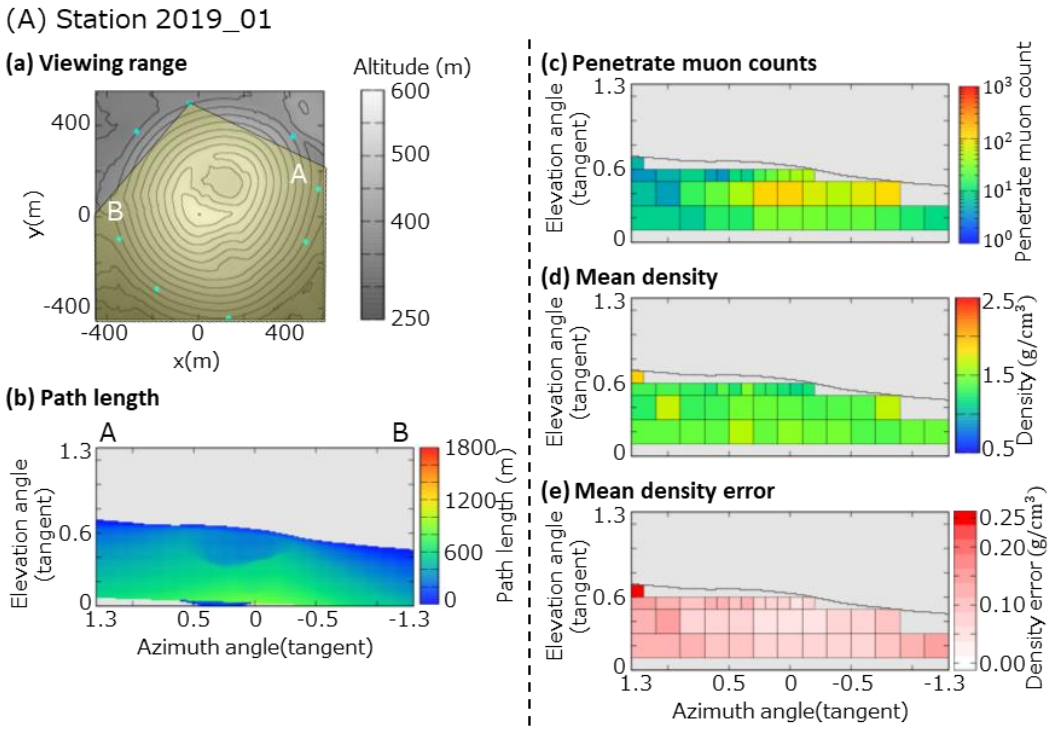

Figure 3.7:(A) The results of muography. (a) Range of view of observed data on DEM. (b) Distribution of path length of mountain body seen from observation point. (c) Muon count through a mountain body. The black line represents the shape of the mountain. The bin size was adjusted so that the muon count was at least 25. (d) Mean density distribution estimated from muography. The numerical table of muon counts used to obtain the mean density was created for a range of densities from 0.5 to 3.0, so bins with observed muon counts outside that range were excluded from the results. (d) Accidental error of mean density distribution estimated from muography.

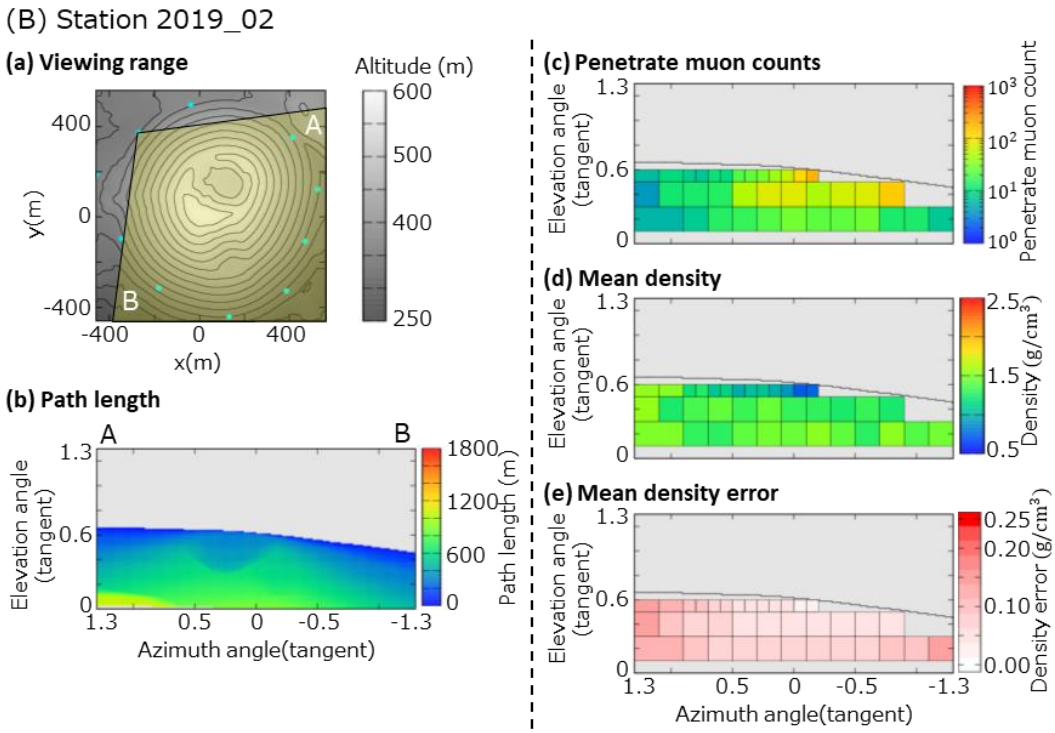

Figure 3.7: (B) The results of muography. (a) Range of view of observed data on DEM. (b) Distribution of path length of mountain body seen from observation point. (c) Muon count through a mountain body. The black line represents the shape of the mountain. The bin size was adjusted so that the muon count was at least 25. (d) Mean density distribution estimated from muography. The numerical table of muon counts used to obtain the mean density was created for a range of densities from 0.5 to 3.0, so bins with observed muon counts outside that range were excluded from the results. (d) Accidental error of mean density distribution estimated from muography.

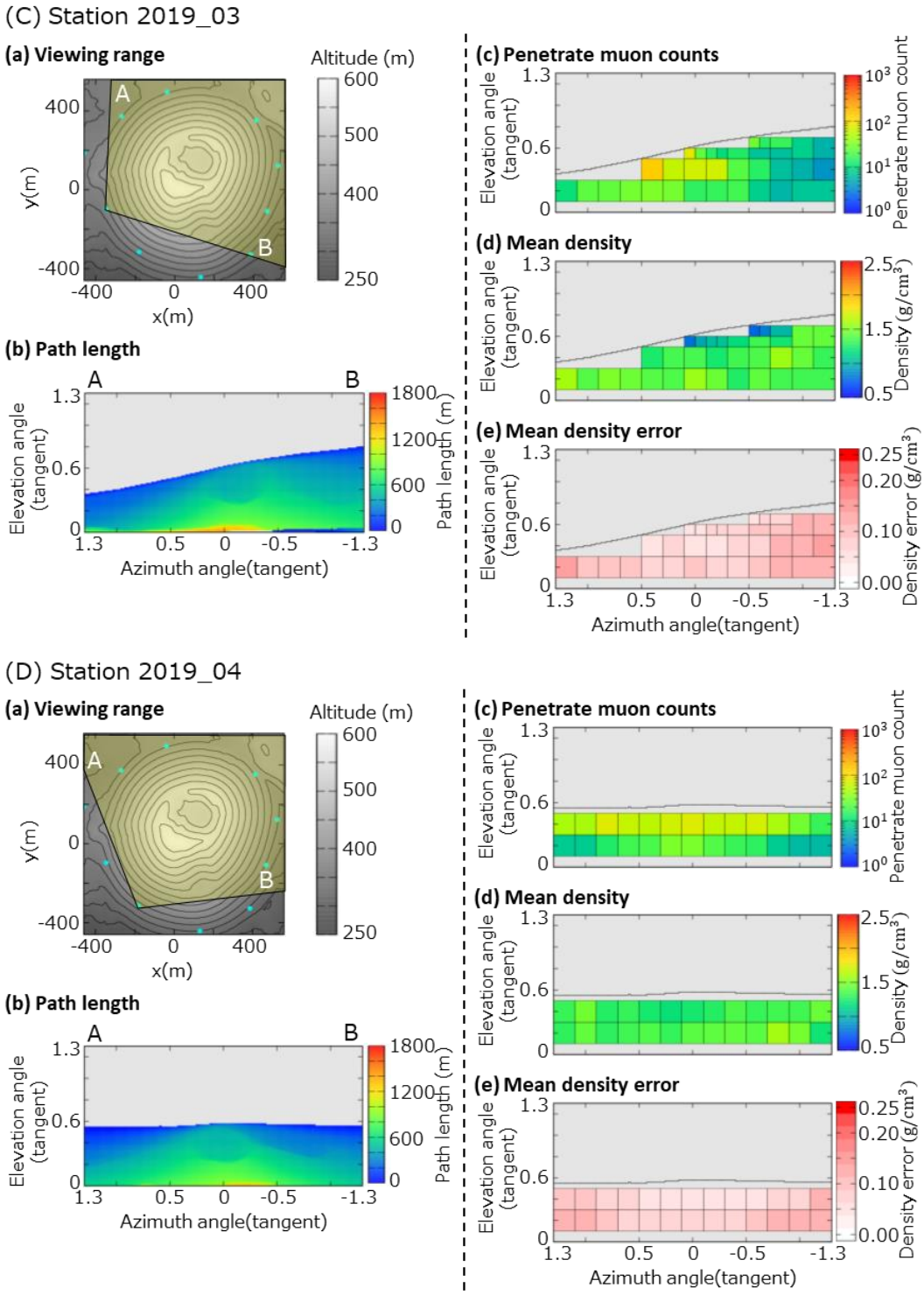

Figure 3.7: (C, D) The results of muography. (a) Range of view of observed data on DEM. (b) Distribution of path length of mountain body seen from observation point. (c) Muon count through a mountain body. The black line represents the shape of the mountain. (d) Mean density distribution estimated from muography. (d) Accidental error of mean density distribution estimated from muography.

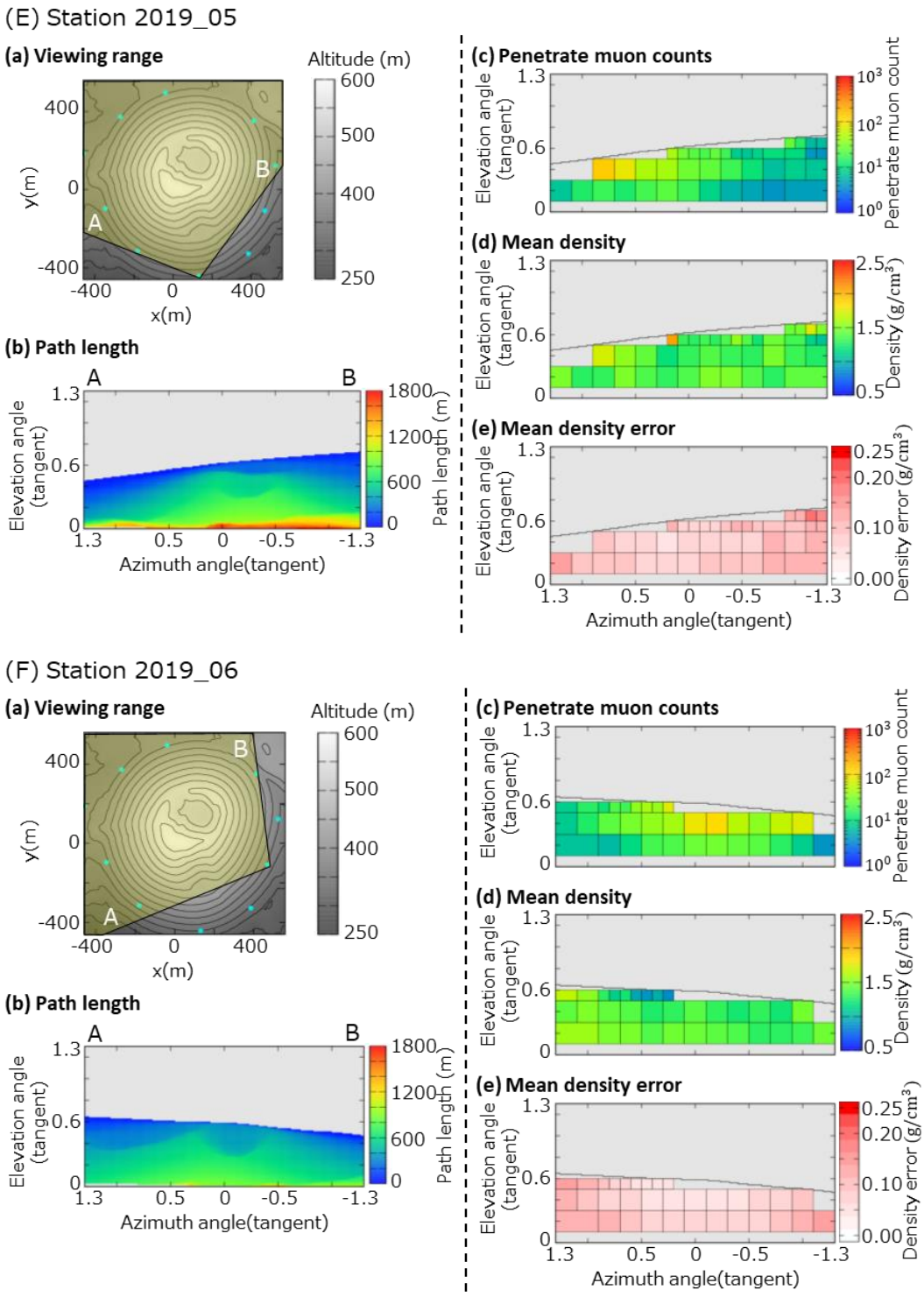

Figure 3.7: (E, F) The results of muography. (a) Range of view of observed data on DEM. (b) Distribution of path length of mountain body seen from observation point. (c) Muon count through a mountain body. The black line represents the shape of the mountain. (d) Mean density distribution estimated from muography. (d) Accidental error of mean density distribution estimated from muography.

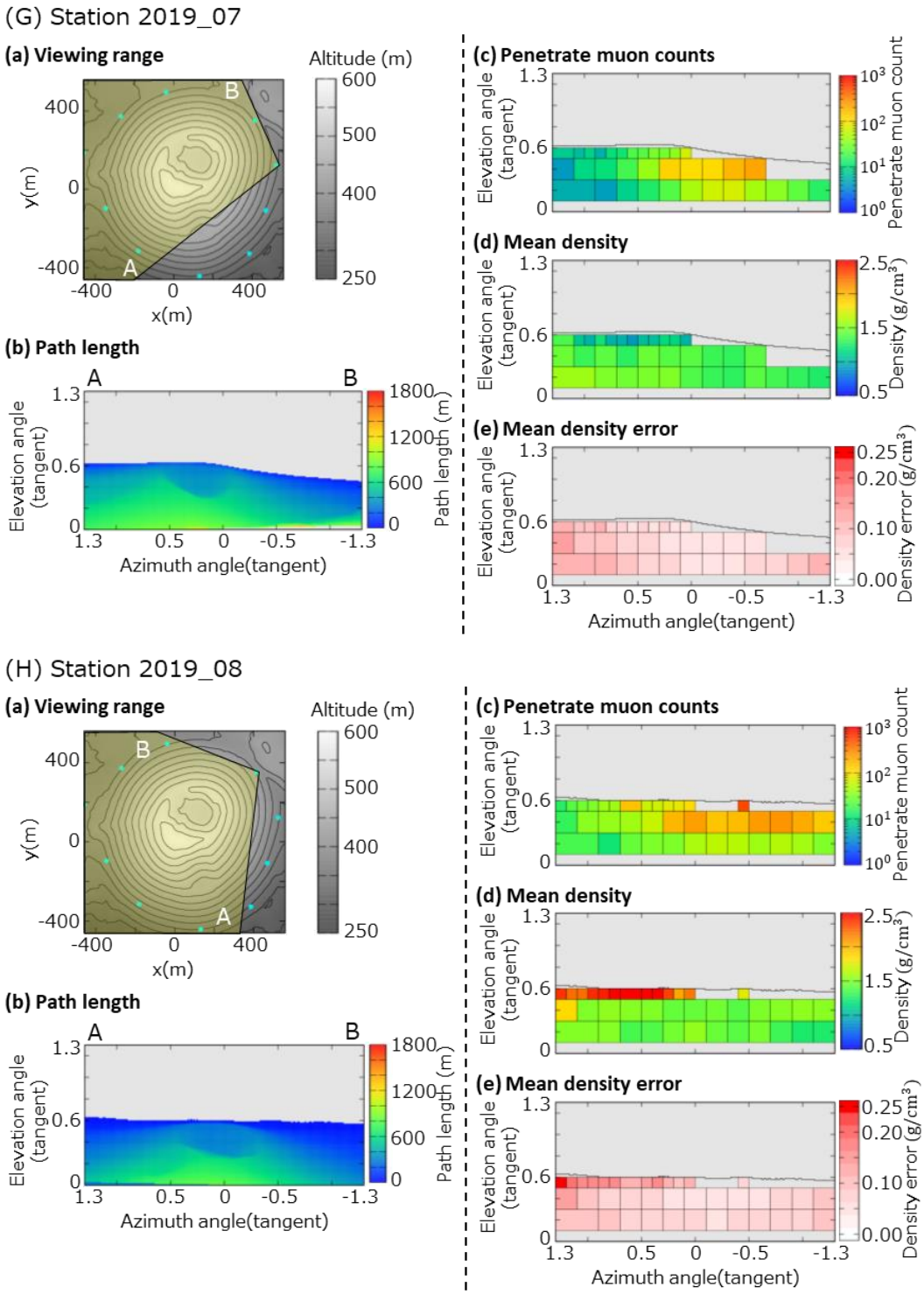

Figure 3.7: (G, H) The results of muography. (a) Range of view of observed data on DEM. (b) Distribution of path length of mountain body seen from observation point. (c) Muon count through a mountain body. The black line represents the shape of the mountain. (d) Mean density distribution estimated from muography. (d) Accidental error of mean density distribution estimated from muography.

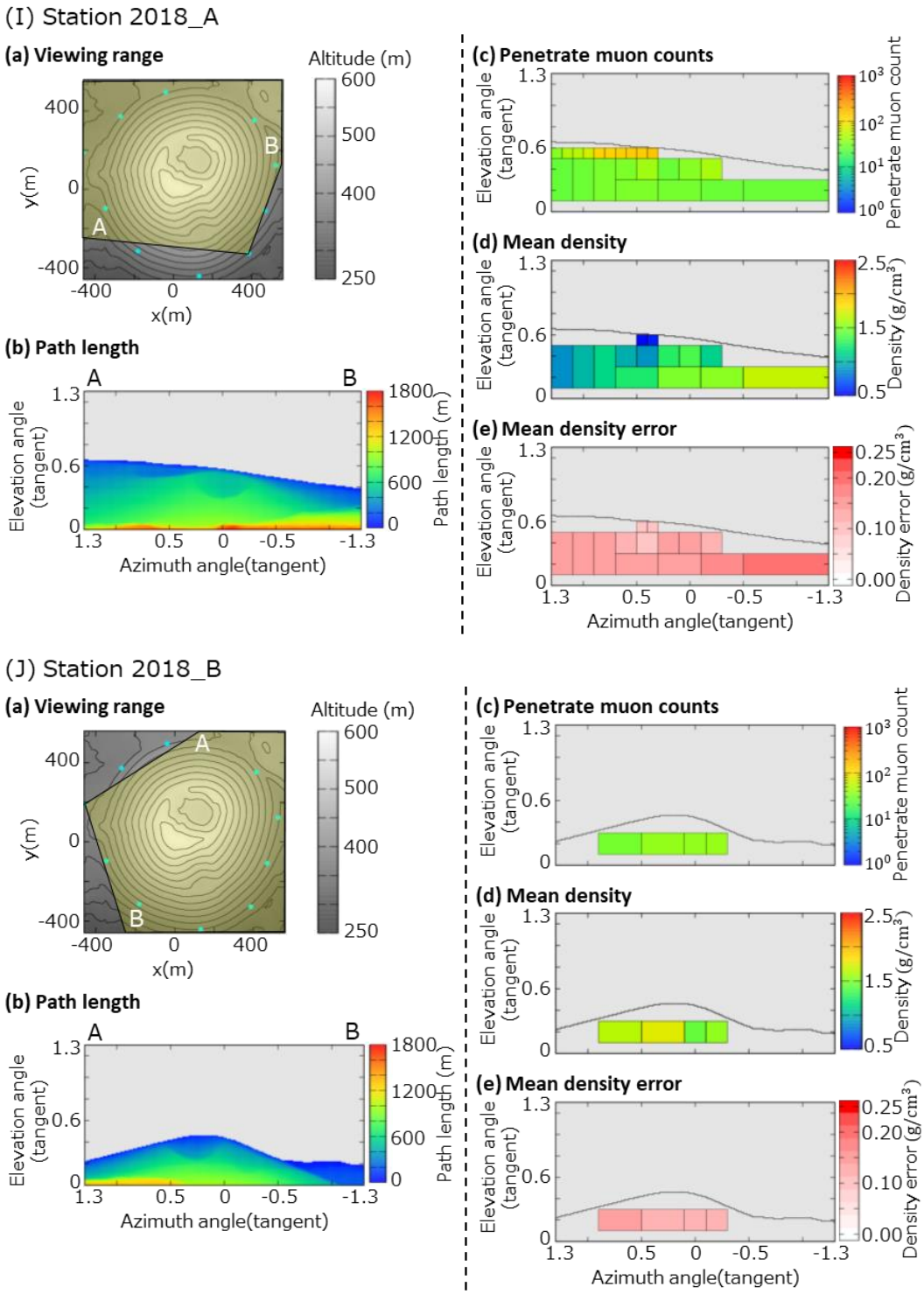

Figure 3.7: (I, J) The results of muography. (a) Range of view of observed data on DEM. (b) Distribution of path length of mountain body seen from observation point. (c) Muon count through a mountain body. The black line represents the shape of the mountain. (d) Mean density distribution estimated from muography. (d) Accidental error of mean density distribution estimated from muography.

3.5. Three-dimensional Density Reconstruction

本節については、5 年以内に雑誌等で刊行予定のため、非公開。

（全文版 P.70～73）

4. Discussion

本章については、5 年以内に雑誌等で刊行予定のため、非公開。

（全文版 P.74～127）

5. Volcanological Discussion

本章については、5 年以内に雑誌等で刊行予定のため、非公開。

（全文版 P.128～131）

6. Future Prospects

This study simplified the muography volcano observation using emulsion. As a result, muography was performed from a total of 11 directions, and 3D density reconstruction was achieved using the observed data from 10 of those directions. However, we could not use 3D density reconstruction with filtered back projection used by Nagahara et al. (2018) in 10 directions. This implies that the resolution of the 3D density reconstruction results can still be improved. Therefore, we will be able to reveal the density structure in more detail by conducting further observations with more observation points.

The newly developed detector and its analysis method have succeeded in simplifying not only multi-directional muography, but also muography itself using emulsion films. This means that more and more people are able to handle muography using emulsion. Therefore, in the future, volcanologists who are not directly specialized in emulsion will be able to actively perform muography.

On the other hand, when conducting multi-directional muography at other volcanoes, there may be limitations on where it can be installed due to topography and eruptive activity. In this case, it is necessary to evaluate how the 3D density reconstruction results will be affected.

The results of this study can be applied to muography for other than volcanoes.

The detector developed in this study can be used for field observation of muography. Therefore, the detector can be used for muography on objects other than volcanoes. For example, some of the targets that have already been observed with previous detectors include the following, cultural assets such as Egyptian pyramids (Morishima et al., 2017b), glacier (Nishiyama et al., 2019). The analysis method for track using a similar detector can also be used without modification when the same detector is used.

The 3D density reconstruction method using muographic data can also be applied to any objects. For example, Morishima et al. (2017b) discovered an unknown cavity in an Egyptian pyramid using muography, but were unable to determine its location exactly. The location and shape of this cavity could be clarified in three dimensions by performing muographic observations from multiple directions and 3D density reconstruction as in this study.

However, there is still insufficient evaluation of the observational conditions required when performing multi-directional muography on a variety of objects. For example, for a given density anomaly to be detected, it is not organized as to the number of observation points required and the analysis parameters to be used for the analysis. When these are organized, they could give very useful information when planning multi-directional muography.

7. Conclusion

In this paper, we developed the elements that were needed to make multi-directional muography a reality. We demonstrated that the developed method can actually realize multi-directional muography.

In Chapter 2, we described what we have developed to realize multi-directional muography. The following were the necessities that were developed to realize multi-directional muography.

A) Development of a detector suitable for multi-point installation and its operation method.
B) Development of a method to select muons for muography from reconstructed tracks.
C) Improved method for 3D density reconstruction.

Section 2.2 describes the development of a detector suitable for multi-directional muography and its operation. First, the development of the detector was described in terms of test observations in 2018. Although the detector used at this time was successful in acquiring observational data, there were several problems in mass producing it for multi-directional muography.

(i) Since the position of the emulsion film and the lead plate was manually aligned, the accuracy was low.
(ii) The pressure to prevent thermal expansion of the emulsion film was manual, and it depended on the operator's senses to determine whether the compression was sufficient or not.
(iii) By June, the temperature of the emulsion film, which is delicate to temperatures above 25 degrees Celsius, was close to 25 degrees Celsius.
(iv) Adjusting the direction and slope of the detector was a manual process. Depending on the environment of the installation site, it was impossible to adjust it, and the installation site was moved.

For the 2019 observations, we developed a detector and operational method that solved these problems and performed the observations. The developed detector has the following features. A frame that unites the nuclear emulsion films and the lead plate for noise reduction was adopted so that the position can be easily adjusted. In order to apply a constant pressure to the emulsion films, a special spring plate was developed. These

were operated in a dedicated container. The container was covered with insulation material to prevent the emulsion films from becoming hot. The attitude of the detector was not adjusted, but rather the attitude at the time of installation was made available for measurement to deal with cases where adjustment was not possible.

In section 2.3, we described how to select the muon tracks to be used in the muography from the analysis data of emulsion films and how to estimate the efficiency of the detector. In section 2.3.1, We described the process of track reconstruction using NETSCAN2.0 and the parameters used in the process. In section 2.3.2, we showed how to select a muon track suitable for the detector used in this study. It was also confirmed that the low-energy muons below 1 GeV, which were shown in Nishiyama et al. (2014b), could be removed by that method. In section 2.3.3, the method of estimating the efficiency for this detector was described.

In section 2.4, improvements to the 3D density reconstruction method were described. This improvement clarified the treatment of areas where voxels are not defined. It became possible to take into account the effect of the spread of the solid angle region in the muon arrival direction.

In Chapter 3, we discussed the results of the demonstration observations. The demonstration observations were performed at a total of 11 locations, three in 2018 and eight in 2019 at Mt. Omuro-yama in Izu Peninsula, Japan.

In section 3.2, the analysis of the muon track data from the observation data was described. In this section, we applied the method described in section 2.3 to actual observation data.

In section 3.3, we compared the simulated muon count with the observed muon count for the free sky part in order to check whether the obtained results were correct. As a result, the observed muon counts were about 10% lower than the simulation. At one of the 2018 stations, the observed muon count was more than 30% lower than the simulated muon count, and there was also a large variation in the ratio from direction to direction. Therefore, the data from this station was excluded from the subsequent analysis. The ratio of the observed muon counts to the simulated muon counts was used as the calibration value.

Using the analyzed muon count data, a two-dimensional muography image was created. We also evaluated the error depending on the muon statistics. We applied the

3D density reconstruction method described in section 2.4 to the observed muon counts to perform 3D density reconstruction.

In Chapter 4, the 3D density reconstruction results were discussed. Specifically, three topics were discussed: the selection of parameters to be used for 3D density reconstruction calculations, the evaluation of errors including systematic errors that depend on the 3D density reconstruction calculation method, and the evaluation of resolution by simulation.

In section 4.1, We discussed the constraints on the correlation length l and a priori error of the density σ_ρ in Nishiyama et al. (2014). For l, we constrained the lower limit to 70m based on the consideration of the amount of information in the data and the amount of information in the reconstruction result. For σ_ρ, we excluded areas with densities of less than 0.5 $(\mathrm{g/cm^3})$ and greater than 3.0 $(\mathrm{g/cm^3})$, which are unlikely to be realistic volcanic densities, and which make up more than 10% of the total. As a result, σ_ρ < 0.5 $(\mathrm{g/cm^3})$ was selected. We also excluded σ = 0.1 because it was too restrictive and the structure did not show up in the 3D density reconstruction results. From the above, σ_ρ= 0.3$(\mathrm{g/cm^3})$ and l = 70m were used to discuss the internal structure. We also confirmed that there was no significant effect on the reconstruction results between l = 70 m and 100 m. We confirmed that between σ_ρ= 0.2$(\mathrm{g/cm^3})$ and 0.4$(\mathrm{g/cm^3})$, the density contrast only changes and the structure does not change.

In section 4.2, we evaluated the error of the density distribution. Three types of errors were evaluated. Section 4.2.1 was to determine the propagation of the error in the observed data, which was determined by the posterior variance matrix in the inversion. The diagonal component of the covariance matrix in the 3D density reconstruction was used for this. In section 4.2.2, we evaluated the effect of the initial density assumed in the inversion. Since the initial density was the value of the bulk density of the mountain obtained from muography data, the error was the change in the 3D reconstruction result when the initial density changed within the error range. In section 4.2.3, The stability of the solution to the choice of data was evaluated. We performed 3D density reconstruction excluding data from one observation point and compared it to the case where data from all observation points were used. As a result, when the observation point is excluded, the density in the vicinity from that point toward the center of the mountain tends to increase. In addition, the density around the point becomes lower. In addition, there was little effect of removing observatories with a small number of

observed muons that were easily visible to other observatories. We interpreted this change in the reconstruction results as a systematic error due to data selection. In section 4.2.4, The variance of the error in the 3D density reconstruction results was defined as the sum of the squares of the above three errors.

In section 4.3, in order to evaluate the spatial resolution of the obtained density structures, we performed simulations assuming two types of structures. The first is the case where a 100m diameter cylinder exists just below the crater. As a result, it was found that the spatial resolution tended to be worse in the lower elevation areas. The second is the case where a plate-like heterogeneity exists from the west to the crater. As a result, the thickness of the plate appeared to spread by a factor of two, and the center side of the mountain body tended to spread more widely.

In section 4.4, The effect of the approximation of the observation matrix on the muon count is discussed. we compared the results with the case where the density distribution assumed when approximating the observation matrix was changed. As a result, it was confirmed that the effect of the error was smaller than the error for the reconstruction results of this study.

In Chapter 5, we interpreted the internal structure of Mt. Omuro-yama and its eruptive history based on the 3D density reconstruction results and previous studies.

The structure confirmed by the results of muography is as follows. A high-density region existed in the central part of the mountain body, and the high-density region extended to the west. A high-density region was also found in the south-southeast. Although the structure is small and could be a ghost, a small area of high density was observed from the center of the mountain to the north-northeast.

From the above, we have constructed a tentative story of the formation process of Mt. Omuro-yama, mainly in its final stages, together with the results of topographic readings. First, when most of the mountain body was formed and a lava lake was formed in the summit crater, the expansion of the mountain body formed a dike that went in three directions from the conduit. Westward dike flowed seeping out from the west side of the mountain. This is consistent with the lava flow IV described in Koyano et al. (1996) and is also consistent with the surrounding topography. The south-southeastward dike erupted a small crater on the south mountainside. Subsequently, most of the lava lake in the summit crater drained back. After the drained

back, the area around the conduit remained hot and the welding progressed to form a high density region in the center of the mountain.

In chapter 6, the future prospects of this research were described. With this research, we have all the detectors, installation techniques, and analysis methods necessary for multi-directional muographic observations. Although the current number of observation directions is only 11, we will increase the number of observation directions by conducting similar observations in the future, and 3D density reconstruction with higher spatial resolution will become possible. In addition, these technologies have made it possible to perform not only multi-directional muography, but also muography itself using nuclear dry plates in a simple manner. This is expected to promote the spread of not only Mt. Omuro-yama, the target of this observation, but also of muography itself.

Acknowledgements

I would like to express my deepest gratitude to the following people for their generous supports.

We would like to thank Dr. Hiroyuki Tanaka for his support and guidance during the entire process of this research. I learned how to handle emulsion films from Dr. Seigo Miyamoto, and he consulted me on all aspects of my research. I received many critically important comments from Dr. Akimichi Taketa. I thank Dr. Ryuichi Nishiyama for allowing me to discuss the methods of 3D density reconstruction with him.

I would like to thank Dr. Yosuke Aoki and Dr. Kiwamu Nishida for giving me the opportunity to experience fieldwork at Usu volcanic region.

We would like to thank Dr. Mitsuhiro Nakamura and Dr. Kunihiro Morishima (F-Lab, Nagoya University) for their help in preparing and developing the emulsion film. Dr. Toshiyuki Nakano gave me a lot of advice on the use of HTS.

We wish to thank Dr. Masato Koyama (Shizuoka University) and Dr. Yusuke Suzuki for their great cooperation in our fieldwork at Mt. Omuro-yama. They have also contributed greatly to the volcanological discussions in this study. I would like to express my deep gratitude to Mr. Masakazu Ichikawa for his great support during the observation at Mt. Omuro-yama. I would also like to thank Mr. Hideaki Aoki for allowing me to observe at Mt. Omuro-yama.

During my PhD program, I have got financial supports from JSPS Fellowship (DC2, 19J13805).

Finally, I wish to thank my parents for supporting me all the time.

References

Alvarez, L. W., Anderson, J. A., El Bedwei, F., Burkhard, J., Fakhry, A., Girgis, A., Goneid, A., Hassan, F., Iverson, D., Lynch, G., Miligy, Z., Moussa, A. H., Sharkawi, M. & Yazolino, L. (1970). Search for hidden chambers in the pyramids. *Science*, **167**(3919), 832-839.

Ambrosino, F., Anastasio, A., Bross, A., Béné, S., Boivin, P., Bonechi, L., ... & D'Alessandro, R. (2015). Joint measurement of the atmospheric muon flux through the Puy de Dôme volcano with plastic scintillators and Resistive Plate Chambers detectors. *Journal of Geophysical Research: Solid Earth*, **120**(11), 7290-7307.

Arrabito, L., Barbuto, E., Bozza, C., Buontempo, S., Consiglio, L., Coppola, D., et al., (2006). Hardware performance of a scanning system for high speed analysis of nuclear emulsions. *Nuclear Instruments and Methods in Physics Research Section A: Accelerators, Spectrometers, Detectors and Associated Equipment*, **568**(2), 578-587.

Barnaföldi, G. G., Hamar, G., Melegh, H. G., Oláh, L., Surányi, G., & Varga, D. (2012). Portable cosmic muon telescope for environmental applications. *Nucl. Instr. Meth*. **A 689**, 60–69 (2012).

Barnoud, A., Cayol, V., Niess, V., Carloganu, C., Lelièvre, P., Labazuy, P., & Le Ménédeu, E. (2019). Bayesian joint muographic and gravimetric inversion applied to volcanoes. *Geophysical Journal International*, **218**(3), 2179-2194.

Calvari, S., Bonaccorso, A., Madonia, P., Neri, M., Liuzzo, M., Salerno, G. G., Behncke, B., Caltabiano, T., Cristaldi, A., Giuffrida, G., La Spina, A., Marotta, E., Ricci, T. & Spampinato, L. (2014). Major eruptive style changes induced by structural modifications of a shallow conduit system: the 2007–2012 Stromboli case. *Bulletin of volcanology*, **76**(7), 1-15.

Carbone, D., Gibert, D., Marteau, J., Diament, M., Zuccarello, L., & Galichet, E. (2014).

An experiment of muon radiography at Mt Etna (Italy). *Geophys. J. Int*., **196**(2), 633-643.

Carloganu, C., Niess, V., Béné, S., Busato, E., Dupieux, P., Fehr, F., Gay, P., Miallier, D., Vulpescu, B., Boivin, P., Combaret, C., Labazuy, P., I. Laktineh, I., Lenat, J. -F., L. Mirabito, L. & Portal, A. (2013). Towards a muon radiography of the Puy de Dôme. *Geosci. Instrum. Method. Data Syst.*, **2**, 55–60, 2013

Cimmino, L., Baccani, G., Noli, P., Amato, L., Ambrosino, F., Bonechi, L., ... & Gonzi, S. (2019). 3d muography for the search of hidden cavities. *Scientific reports*, **9**(1), 1-10.

Cosburn, K., Roy, M., Guardincerri, E., & Rowe, C. (2019). Joint inversion of gravity with cosmic ray muon data at a well-characterized site for shallow subsurface density prediction. *Geophysical Journal International*, **217**(3), 1988-2002.

Geshi, N., & Neri, M. (2014). Dynamic feeder dyke systems in basaltic volcanoes: the exceptional example of the 1809 Etna eruption (Italy). *Frontiers in Earth Science*, **2**, 13.

Giudicepietro, F., D'Auria, L., Martini, M., Caputo, T., Peluso, R., De Cesare, W., ... & Scarpato, G. (2009). Changes in the VLP seismic source during the 2007 Stromboli eruption. *Journal of volcanology and geothermal research*, **182**(3-4), 162-171.

Groom, D. E., Mokhov, N. V. & Striganov, S. I. (2001). Muon Stopping Power and Range Tables 10 MeV–100 TeV, *Atom. Data Nucl. Data Tab.*, **78**, 183–356, 2001.

Hamada, K., Fukuda, T., Ishiguro, K., Kitagawa, N., Kodama, K., Komatsu, M., Morishima, K., Nakano, T., Nakatsuka, Y., Nonoyama, Y., Sato, O. & Yoshida, J. (2012). Comprehensive track reconstruction tool “NETSCAN 2.0” for the analysis of the OPERA Emulsion Cloud Chamber. *Journal of Instrumentation*, **7**(07), P07001.

Hamuro, K. (1986). Petrology of the Higashi-Izu monogenetic volcano group. *Bulletin of the Earthquake Research Institute, University of Tokyo*, **60**(3), 335-400.

Honda, M., Kajita, T., Kasahara, K. & Midorikawa, S., (2004). New calculation of the atmospheric neutrino flux in a three-dimensional scheme, *Phys. Rev. D*, **70**, 043008

Hotta, K., (2019). Study on Magma Accumulation and Migration Based on Combined Ground Deformation Data in and around Sakurajima Volcano, *Volcanol. Soc. Jpn*., **64,** 3, 175.

Jourde, K., Gibert, D., & Marteau, J. (2015). Improvement of density models of geological structures by fusion of gravity data and cosmic muon radiographies. *Geoscientific Instrumentation, Methods and Data Systems*, **4**, 177-188.

Jourde, K., Gibert, D., Marteau, J., de Bremond d'Ars, J., & Komorowski, J. C. (2016). Muon dynamic radiography of density changes induced by hydrothermal activity at the La Soufrière of Guadeloupe volcano. *Scientific reports*, **6**(1), 1-12.

Koyaguchi, T., Suzuki, Y. J., Takeda, K., & Inagawa, S. (2018). The condition of eruption column collapse: 2. Three‐dimensional numerical simulations of eruption column dynamics. *Journal of Geophysical Research: Solid Earth*, **123**(9), 7483-7508.

Koyano, Y., Hayakawa, Y., & Machida, H. (1996). The Eruption of Omuroyama in the Higashi Izu Monogenetic Volcano Field. *Journal of Geography (Chigaku Zasshi)*, **105**(4), 475-484.

Lesparre, N., Gibert, D., Marteau, J., Komorowski, J.C., Nicollin, F. & Coutant, O. (2012). Density muon radiography of La Soufrière of Guadeloupe volcano-comparison with geological, electrical resistivity and gravity data, *Geophys. J. Int*. **190**, 1008–1019.

Minato, S. (1986). Bulk density estimates of buildings using cosmic rays. *International*

Journal of Radiation Applications and Instrumentation. Part A. Applied Radiation and Isotopes, **37**(9), 941-946.

Miyamoto, S., Barrancos, J., Bozza, C., Consiglio, L., De Sio, C., Hernández, P., Nishiyama, R., Padilla, G., Padrón, E., Sirignano, C., Stellacci, S. M., Tanaka, H. K. M. & Tioukov, V. (2017). Muography of 1949 fault in La Palma, Canary Islands, Spain. *Annals of Geophysics*, **60**(1), 0110.

Morishima, K., Nishio, A., Moto, M., Nakano, T., & Nakamura, M. (2017a). Development of nuclear emulsion for muography. *Annals of Geophysics*, **60**(1), 0112.

Morishima, K., Kuno, M., Nishio, A., Kitagawa, N., Manabe, Y., Moto, M., ... & Hayashi, K. (2017b). Discovery of a big void in Khufu's Pyramid by observation of cosmic-ray muons. *Nature*, **552**(7685), 386-390.

Nagahara, S., & Miyamoto, S. (2018). Feasibility of three-dimensional density tomography using dozens of muon radiographies and filtered back projection for volcanos. *Geoscientific Instrumentation, Methods and Data Systems*, **7**(4), 307-316.

Nagamine, K., Iwasaki, M., Shimomura, K., & Ishida, K. (1995). Method of probing inner-structure of geophysical substance with the horizontal cosmic-ray muons and possible application to volcanic eruption prediction. *Nuclear Instruments and Methods in Physics Research Section A: Accelerators, Spectrometers, Detectors and Associated Equipment*, **356**(2-3), 585-595.

Nagamine, K., Tanaka, H. K., Nakamura, S. N., Ishida, K., Hashimoto, M., Shinotake, A., Naito, M. & Hatanaka, A. (2005). Probing the inner structure of blast furnaces by cosmic-ray muon radiography. *Proceedings of the Japan Academy, Series B*, **81**(7), 257-260.

Nakamichi, H., Watanabe, H., & Ohminato, T. (2007). Three‐dimensional velocity

structures of Mount Fuji and the South Fossa Magna, central Japan. *Journal of Geophysical Research: Solid Earth,* **112**(B3).

Nakamichi, H., Yamamoto, K., Yamada, T., Tameguri, T., Takahashi, K., Aoyama, H., ... & Osuga, K. (2020). Active Seismic Source Experiment in Sakurajima Volcano in 2019 and Comparison with the Previous Experiments. *Disaster Prevention Research Institute Annuals*. B, **63**(B), 100-107.

Nishio, A., Morishima, K., Kuwabara, K. I., Yoshida, T., Funakubo, T., Kitagawa, N., Kuno, M., Manabe, Y. & Nakamura, M. (2020). Nuclear emulsion with excellent long-term stability developed for cosmic-ray imaging. *Nuclear Instruments and Methods in Physics Research Section A: Accelerators, Spectrometers, Detectors and Associated Equipment*, **966**, 163850.

Nishiyama, R., Tanaka, Y., Okubo, S., Oshima, H., Tanaka, H.K. M. & Maekawa, T., (2014a). Integrated processing of muon radiography and gravity anomaly data toward the realization of high-resolution 3-D density structural analysis of volcanoes: Case study of Showa-Shinzan Lava Dome, Usu, Japan, *Journal of Geophysical Research Solid Earth*, **119**, 699–710.

Nishiyama, R., Miyamoto, S., & Naganawa, N. (2014b). Experimental study of source of background noise in muon radiography using emulsion film detectors. *Geoscientific Instrumentation, Methods and Data Systems*, **3**(1), 29.

Nishiyama, R., Taketa, A., Miyamoto, S., & Kasahara, K. (2016). Monte Carlo simulation for background study of geophysical inspection with cosmic-ray muons. *Geophysical Journal International*, **206**(2), 1039-1050.

Nishiyama, R., Miyamoto, S., Okubo, S., Oshima, H. & Maekawa, T. (2017). 3D Density Modeling with Gravity and Muon-Radiographic Observations in Showa-Shinzan Lava Dome, Usu, Japan, *Pure and Applied Geophysics*, doi:10.1007/s00024-016-1430-9.

Nishiyama, R., Ariga, A., Ariga, T., Lechmann, A., Mair, D., Pistillo, C., Scampoli, P., Valla, P. G., Vladymyrov, M. & Schlunegger, F. (2019). Bedrock sculpting under an active alpine glacier revealed from cosmic-ray muon radiography. *Scientific reports*, **9**(1), 1-11.

Oláh, L., Tanaka, H. K., Ohminato, T., & Varga, D. (2018). High-definition and low-noise muography of the Sakurajima volcano with gaseous tracking detectors. *Scientific reports*, **8**(1), 1-13.

Rosas-Carbajal, M., Jourde, K., Marteau, J., Deroussi, S., Komorowski, J. C., & Gibert, D. (2017). Three-dimensional density structure of La Soufrière de Guadeloupe lava dome from simultaneous muon radiographies and gravity data. *Geophysical Research Letters*, **44**(13), 6743-6751.

Saito, T., Takahashi, S., & Wada, H. (2003). 14 C ages of Omuroyama volcano, Izu Peninsula. *Kazan*, **48**(2), 215-219.

Saracino, G., Ambrosino, F., Bonechi, L., Bross, A., Cimmino, L., Ciaranfi, R., Raffaello D'Alessandro, R. D., Giudicepietro, F., Macedonio, G., Martini, M., Masone, V., Mori, M., Noli, P., Orazi, M., Passeggio, G., Pla-Dalmau, A., Roscilli, L. & Strolin, P. (2017). The MURAVES muon telescope: technology and expected performances. *Annals of Geophysics*, **60**(1), 0103.

Suzuki, Y. J., & Koyaguchi, T. (2009). A three‐dimensional numerical simulation of spreading umbrella clouds. *Journal of Geophysical Research: Solid Earth*, **114**(B3).

Suzuki, Y., Koyama, M. & Sugimoto, N. (2020). VIRTUAL SHIZUOKA で見る伊豆東部火山群，日本火山学会 2020 年秋季大会，P-17，Online

Tanaka, H. K. M., Nakano, T., Takahashi, S., Takeo, M., Oikawa, J., Ohminato, T., Aoki, Y., Koyama, E., Tsuji, H. & Niwa, K. (2007a). High resolution imaging in the inhomogeneous crust with cosmic-ray muon radiography: The density structure

below the volcanic crater floor of Mt.Asama, *Japan, Earth Planet. Sci. Lett*., doi:10.1016/j.epsl.2007.09.001.

Tanaka, H. K. M., Nakano, T., Takahashi, S., Yoshida, J., Ohshima, H., Maekawa, T., Watanabe, H. & Niwa, K. (2007b). Imaging the conduit size of the dome with cosmic-ray muons: The structure beneath Showa-Shinzan Lava Dome, *Japan, Geophys. Res. Lett.*, **34**, L22311.

Tanaka, H. K. M., Uchida, T., Tanaka, M., Shinohara, H. & Taira, H. (2009). Cosmic-ray muon imaging of magma in a conduit: Degassing process of Satsuma-Iwojima Volcano, Japan, *Geophys. Res. Lett.*, **36**, L01304.

Tanaka, H. K. M., Taira, H., Uchida, T., Tanaka, M., Takeo, M., Ohiminato, T. & Tsuji, H. (2010). Three-dimensional computational axial tomography scan of a volcano with cosmic ray muon radiography, *J. Geophys. Res.*, **115**, B12332, 2010.

Tanaka, H. K., Miyajima, H., Kusagaya, T., Taketa, A., Uchida, T., & Tanaka, M. (2011). Cosmic muon imaging of hidden seismic fault zones: Rainwater permeation into the mechanical fractured zones in Itoigawa–Shizuoka Tectonic Line, Japan. *Earth and Planetary Science Letters*, **306**(3-4), 156-162.

Tanaka, H.K.M., Kusagaya, T. & Shinohara, H. (2014). Radiographic visualization of magma dynamics in an erupting volcano, *Nature Communications,* **5**, Article number: 3381 (2014) doi:10.1038/ncomms4381.

Tarantola, A., & Valette, B. (1982). Inverse problems= quest for information. *Journal of geophysics*, **50**(1), 159-170.

Tarantola, A., & Nercessian, A. (1984). Three-dimensional inversion without blocks. *Geophysical Journal International*, **76**(2), 299-306.

Tioukov, V., Kreslo, I., Petukhov, Y., & Sirri, G. (2006). The FEDRA—Framework for emulsion data reconstruction and analysis in the OPERA experiment. *Nuclear*

Instruments and Methods in Physics Research Section A: Accelerators, Spectrometers, Detectors and Associated Equipment, **559**(1), 103-105.

Tioukov, V., De Lellis, G., Strolin, P., Consiglio, L., Sheshukov, A., Orazi, M., Peluso, R., Bazza, C., De Sio, C., Stellacci, S.M., Sirignano, C., D'Ambrosio, N., Miyamoto, S., Nishiyama, R. & Tanaka, H.K.M (2017). Muography with nuclear emulsions-Stromboli and other projects. *Annals of Geophysics*, **60**(1), 0111

Wilson, L., Sparks, R. S. J., & Walker, G. P. (1980). Explosive volcanic eruptions—IV. The control of magma properties and conduit geometry on eruption column behaviour. *Geophysical Journal International*, **63**(1), 117-148.

Yamamoto, H. (2003). The mode of lava outflow from cinder cones in the Ojika-Jima Monogenetic Volcano Group. *Kazan*, **48**(1), 11-25.

Yoshimoto, M., Nakano, T., Komatani, R., & Kawahara, H. (2017). Hyper-track selector nuclear emulsion readout system aimed at scanning an area of one thousand square meters. *Progress of Theoretical and Experimental Physics*, **10**, 2017.

Zyla, P. A. et al. (Particle Data Group), (2020). Review of Particle Physics, *Prog. Theor. Exp. Phys*., **083C01** (2020)